SCIENCE CHINA
Earth Sciences

•ARTICLE•

July 2024 Vol.67 No.7: 2326–2351
https://doi.org/10.1007/s11430-023-1300-9

High-resolution tsunami hazard assessment for the Guangdong-Hong Kong-Macao Greater Bay Area based on a non-hydrostatic tsunami model

Yifan ZHU[1], Chao AN[1*], Houyun YU[2], Wei ZHANG[2] & Xiaofei CHEN[2]

[1] *Key Laboratory of Hydrodynamics (Ministry of Education), School of Ocean and Civil Engineering, Shanghai Jiao Tong University, Shanghai 200240, China;*
[2] *Department of Earth and Space Sciences, Southern University of Science and Technology, Shenzhen 518055, China*

Received September 7, 2023; revised January 25, 2024; accepted March 15, 2024; published online June 19, 2024

Abstract The Guangdong-Hong Kong-Macao Greater Bay Area (GBA) is threatened by potential tsunami hazards from the Littoral Fault Zone (LFZ) and the Manila subduction zone (MSZ), and may suffer huge damage because of its dense population, concentrated infrastructure, and low-lying coasts. Previous tsunami studies for the GBA made simple assumptions on the mechanisms of LFZ earthquakes, and used coarse bathymetry data in tsunami simulation, which limited the prediction of detailed tsunami hazard characteristics. In this paper, we develop a parallel dispersive tsunami model PCOMCOT to efficiently simulate dispersive, nonlinear, and breaking tsunami waves. We also construct large-scale and high-resolution bathymetry models for the GBA by correcting and integrating various data sources. Dynamic rupture simulation is performed for the LFZ to obtain a more reliable earthquake source model. We propose several representative earthquake scenarios for the LFZ and MSZ, and use PCOMCOT to calculate the resulting tsunami waves, currents, and inundation in the GBA. Our results indicate that if an M_w7.5 oblique-slip earthquake occurs in the LFZ off the Pearl River Estuary (PRE), the subsequent tsunami will primarily impact Hong Kong, causing maximum positive and negative waves of around 1 m and −2 m, respectively, along with slightly destructive currents (⩾1.5 m/s). An M_w9.0 MSZ megathrust earthquake can lead to widespread inundation with >1 m depth on the outlying islands of Macao and in the urban areas of Hong Kong around the Victoria Harbour. Besides, it will also cause catastrophic tsunami currents along the narrow waterways in Hong Kong and Macao, and the spatial distribution of strong currents (⩾3 m/s) shows a considerable discrepancy from the areas of serious inundation. Thus, more attention should be paid to the potential impacts of tsunami currents on the GBA.

Keywords Tsunami hazards, Inundation, Tsunami currents, Non-hydrostatic model, Guangdong-Hong Kong-Macao Greater Bay Area

Citation: Zhu Y, An C, Yu H, Zhang W, Chen X. 2024. High-resolution tsunami hazard assessment for the Guangdong-Hong Kong-Macao Greater Bay Area based on a non-hydrostatic tsunami model. Science China Earth Sciences, 67(7): 2326–2351, https://doi.org/10.1007/s11430-023-1300-9

1. Introduction

The Pearl River Delta (PRD) is the largest alluvial plain in Southern China, accommodating one of the most extensive and densely populated urban agglomerations in the world. The Guangdong-Hong Kong-Macao Greater Bay Area (GBA), composed of cities such as Hong Kong, Macao, Guangzhou, Shenzhen, and Zhuhai, serves as a global hub for manufacturing, finance, and international trade. The GBA is potentially threatened by tsunamis from the South China Sea (SCS), and is highly vulnerable to tsunami hazards because of its dense population, concentrated infrastructure, and low-lying coasts (Li et al., 2022a). To ensure

* Corresponding author (email: anchao@sjtu.edu.cn)

the social security of the GBA, the potential tsunami hazards have to be considered in urban planning and disaster mitigation strategies. Thus, it is imperative to conduct detailed tsunami hazard assessment for this area, which provides necessary data for the above purposes.

In the SCS, The Manila subduction zone (MSZ) has the potential to induce serious regional tsunamis, and has long been the focus of tsunami hazard assessments and warning (e.g., Liu et al., 2009; Liu et al., 2015). Megawati et al. (2009) presented an M_w9.0 worst-case rupture model based on the maximum possible slip deficit along the entire MSZ since the 1560s, and simulated the triggered tsunami waves. They showed that the coasts of Guangdong and Fujian provinces are severely affected due to the focusing effects of bathymetry, and that Hong Kong could be hit by waves of up to 6 m. Liu et al. (2009) specified several M_w8.0 earthquake scenarios, following the segmentation of the MSZ proposed by the United States Geological Survey (USGS). They suggested that the distribution of tsunami hazards in the SCS is sensitive to the rupture location, with ruptures in the northern segment of the MSZ being the most dangerous to Southern China. In addition to the scenario-based deterministic hazard assessments, considerable advances have been made in the methodology of probabilistic tsunami hazard assessment (PTHA) for the MSZ. PTHA incorporates various uncertainties in earthquake sources and tsunami propagation, such as earthquake magnitude and location (Liu et al., 2007), coseismic slip distribution (Li et al., 2016; Sepúlveda et al., 2019), climate-driven sea level change (Li et al., 2018; Sepúlveda et al., 2021), etc. The stochastic nature of tsunami hazards is described as exceeding probabilities of different wave height or inundation levels.

Beside the MSZ, the GBA is also threatened by earthquake-generated tsunamis from the nearby Littoral Fault Zone (LFZ). The LFZ is a major intraplate deformation zone stretching over 1000 km along the shoreline of Southern China (Liu, 1981). Because the LFZ is located in the shallow water, most researchers focus only on the associated seismic hazards and ignore the tsunami hazards. In recent years, several historical tsunami events related to the LFZ were discovered (Xu, 2007; Peng et al., 2017), and more attention was paid to its tsunami risk. The LFZ has been included as a source zone of local tsunamis in some PTHA studies (Wen et al., 2011; Ren et al., 2017; Yuan et al., 2021). Previous studies simply assumed the tsunami sources in the LFZ to be pure thrust earthquakes, resulting in relatively severe tsunami hazards (e.g., Ren et al., 2017; Yuan et al., 2021; Li et al., 2022b). However, both the tectonics and the earthquake records of LFZ show that, the fault mechanism changes gradually from oblique thrust faulting to oblique normal faulting from the east to west (Chen and Huang, 1989; Xu et al., 2010; Sun et al., 2012; Peng et al., 2017). Since the tsunamigenic potential of earthquakes strongly depends on their focal mechanisms, more reliable earthquake source models accounting for the tectonic stress and rupture dynamics of LFZ, should be applied in tsunami hazard assessment.

The coastal topography of the GBA is highly complex, characterized by various natural features including islands, bays, channels, etc., and numerous artificial structures such as ports, piers, and breakwaters. As small-scale topographic features significantly influence tsunami propagation and inundation in coastal areas, high-resolution bathymetry data are necessary for accurate modeling of tsunami hazards in the GBA. Most previous studies used publicly available bathymetry data such as the Earth Topography (ETOPO) and General Bathymetric Chart of the Oceans (GEBCO) for tsunami simulation (Liu et al., 2007; Liu et al., 2009; Li et al., 2016; Yuan et al., 2021). These datasets are too coarse (grid size ~15 arc sec) to resolve the small-scale features. The importance of high-resolution bathymetry data is illustrated by Heidarzadeh and Gusman (2021), who simulated the Mediterranean tsunami triggered by the May 20, 2020 M_w6.6 Crete earthquake. They found that the tsunami waves in two ports calculated using GEBCO disagreed with the tide gauge recordings, with the maximum wave height underestimated by ~60%. In comparison, these waves were satisfactorily reproduced using the 3-m resolution grids of the local bathymetry, where the piers and breakwaters are well resolved. By far, a few studies have utilized high-resolution bathymetry data for tsunami inundation modeling in the GBA, focusing on specific ports or islands (e.g., Li et al., 2018; Sepúlveda et al., 2019). For practical applications such as urban planning and emergency management, large-scale and high-resolution bathymetry models need to be constructed for the GBA, based on which detailed distribution of tsunami hazards and city-wide inundation maps can be computed.

Tsunami hazard assessments typically use the shallow water equations for tsunami simulation (An, 2021). For example, the shallow water model COMCOT (Cornell Multigrid Coupled Tsunami Model) (Liu et al., 1998; Wang and Liu, 2006; An et al., 2014) has been widely adopted in tsunami studies for the SCS (e.g., Liu et al., 2009; Li et al., 2016; Ren et al., 2017; Sepúlveda et al., 2019). Due to the small fault size of the LFZ and the possible shallow rupture in the MSZ, earthquakes in these zones can generate shorter tsunami waves, which may be affected by frequency dispersion in long-distance propagation (Glimsdal et al., 2013). Considering that almost all the previous tsunami simulations for the GBA used the shallow water equations, it is important to assess whether the effects of wave dispersion are significant. Most commonly used dispersive tsunami models are based on the Boussinesq-type equations (Peregrine, 1967; Nwogu, 1993; Madsen et al., 1997). Due to the higher-order derivatives in the dispersive terms, it is challenging to

numerically solve these equations. Baba et al. (2015) expressed the dispersive terms for constant water depth with conserved variables (i.e., volume flux), which improved the numerical stability. For non-uniform water depth, the higher-order derivatives of non-conserved variables are unavoidable, and complicated schemes such as shock-capturing schemes and the TVD finite-volume method have to be employed (Shi et al., 2012; Huang et al., 2023). These complex schemes are much more time-consuming, and significantly reduce the computational efficiency. Another type of dispersive model called depth-integrated non-hydrostatic model, has comparable accuracy to the classical Boussinesq equations, but has no higher-order derivatives in the governing equations. This model can be solved efficiently and stably with a semi-implicit scheme (Stelling and Zijlema, 2003; Yamazaki et al., 2009), and has been used in many real events for modeling dispersive tsunamis (e.g., Lay et al., 2011; Bai et al., 2014; Aranguiz et al., 2019). Here, we develop our dispersive tsunami numerical model based on the depth-integrated non-hydrostatic model, and apply it to the high-resolution tsunami hazard assessment for the GBA.

In this paper, we first derive the governing equations of the depth-integrated non-hydrostatic model through theoretical analysis. By combining the solution schemes with the shallow water model COMCOT, the parallel dispersive tsunami model PCOMCOT (Parallelized COMCOT) is developed. Our new model is then validated in a series of numerical tests. For computation of tsunami hazards in the GBA, we construct a high-resolution bathymetry dataset for the PRD, the Hong Kong Special Administrative Region (SAR), and the Macao SAR. Several representative earthquake source models for the LFZ and MSZ are proposed based on dynamic rupture simulation, historical records, and geodetic data. Finally, the tsunami waves, currents, and inundation in the GBA are calculated, and the characteristics of tsunami hazards under these representative scenarios are analyzed in detail.

2. Dispersive tsunami model PCOMCOT

In this section, we first derive the governing equations of the depth-integrated non-hydrostatic model through theoretical analysis. Then, the numerical methods we use for tsunami simulation are described, with a main focus on the semi-implicit scheme for solving wave dispersion. All the numerical schemes are parallelized with the MPI library for high-performance computing. The newly developed tsunami model PCOMCOT can efficiently compute the entire life span of nonlinear, dispersive, and breaking tsunami waves. For model validation, we conduct a series of numerical tests, including the run-up of solitary wave on a circular island and the 2011 Tohoku earthquake tsunami. The numerical results agree satisfactorily with analytical solutions, experimental data, and real tsunami records.

2.1 Governing equations

In a free surface flow, the water pressure can be decomposed into a hydrostatic part p_{sta} caused by the gravity, and a non-hydrostatic part p_{dyn} related with vertical motion, that is

$$p=\rho\left(p_{\mathrm{sta}}+p_{\mathrm{dyn}}\right)=\rho\left[g(\eta-z)+p_{\mathrm{dyn}}\right], \tag{1}$$

in which η is the surface elevation, g is the gravitational acceleration, and the pressure components p_{sta} and p_{dyn} are normalized by the water density ρ. Based on the pressure decomposition, the 3D Navier-Stokes equations for inviscid incompressible flows are expressed as

$$\nabla\cdot\mathbf{u}+\frac{\partial w}{\partial z}=0, \tag{2}$$

$$\frac{\partial\mathbf{u}}{\partial t}+\mathbf{u}\cdot\nabla\mathbf{u}+w\frac{\partial\mathbf{u}}{\partial z}+g\nabla\eta+\nabla p_{\mathrm{dyn}}=0, \tag{3}$$

$$\frac{\partial w}{\partial t}+\mathbf{u}\cdot\nabla w+w\frac{\partial w}{\partial z}+\frac{\partial p_{\mathrm{dyn}}}{\partial z}=0, \tag{4}$$

where $\mathbf{u}$ and w denote the horizontal and vertical velocity components, respectively. Note that the gradient operator ∇ works only in the horizontal direction. The kinematic and dynamic boundary conditions at the free surface and the seabed are

$$\frac{\partial\eta}{\partial t}+\mathbf{u}\cdot\nabla\eta-w=0,\ z=\eta(x,y,t), \tag{5}$$

$$\mathbf{u}\cdot\nabla h+w=0,\ z=-h(x,y), \tag{6}$$

$$p_{\mathrm{dyn}}=0,\ z=\eta(x,y,t), \tag{7}$$

in which h is the still water depth. In order to derive the 2D governing equations for tsunami modeling, we need to simplify eqs. (2)–(4) based on the characteristics of tsunami waves and the boundary conditions in eqs. (5)–(7), and then integrate the simplified equations along the vertical direction.

In general, tsunamis are weakly nonlinear and moderately dispersive waves, i.e., the two small parameters $\varepsilon=A/h_0$ and $\mu=kh_0$ satisfy the condition $O(\varepsilon)\approx O(\mu^2)\ll 1$, where A is the wave amplitude, h_0 is the characteristic water depth, and k is the wavenumber (Mei, 1989). Here, we consider only the terms up to $O(\varepsilon,\mu^2)$, which is the same as the classical Boussinesq equations. By integrating the 3D continuity equation (eq. (2)) along the z-direction and applying the kinematic boundary conditions (eqs. (5) and (6)), the 2D continuity equation for calculating surface elevation is given as

$$\frac{\partial\eta}{\partial t}+\nabla\cdot\mathbf{F}=0. \tag{8}$$

Here $\mathbf{F}$ is the horizontal volume flux defined as $\mathbf{F}=\int_{-h}^{\eta}\mathbf{u}\mathrm{d}z=\overline{\mathbf{u}}(\eta+h)$, where $\overline{\mathbf{u}}$ is the depth-averaged hor-

izontal velocity, i.e., $\overline{\mathbf{u}} = (\eta + h)^{-1}\int_{-h}^{\eta} \mathbf{u}\mathrm{d}z$. Neglecting the terms of orders higher than $O(\varepsilon,\mu^2)$ in eqs. (3)–(4) and integrating them over total water depth, we obtain the following depth-integrated momentum equations.

$$\frac{\partial \mathbf{F}}{\partial t} + \nabla\cdot\left(\frac{\mathbf{FF}}{D}\right) + gD\nabla\eta + \nabla\left(\int_{-h}^{\eta} p_{\mathrm{dyn}}\,\mathrm{d}z\right) - q\nabla h = 0, \tag{9}$$

$$\frac{\partial W}{\partial t} = \frac{q}{D}, \tag{10}$$

where **FF** is a dyadic tensor (i.e., the outer product of **F** and itself), $D=\eta+h$ is the total water depth, q represents the non-hydrostatic pressure at the bottom, and W is the depth-averaged vertical velocity. For moderately dispersive waves, the vertical velocity w varies linearly along the z-direction (Peregrine, 1967; Nwogu, 1993), so W is simply the average value of w at the free surface and the bottom given by eqs. (5) and (6). Note that the Leibniz rule and the dynamic boundary condition in eq. (7) are used in the integration of ∇p_{dyn}. Eqs. (9) and (10) have the same accuracy as the classical Boussinesq equations but cannot be solved yet, because the integration of p_{dyn} is not given. A reasonable approximation of p_{dyn} is needed for estimating this integration.

The expression of p_{dyn} corresponding to the classical Boussinesq equations is given by Peregrine (1967) as

$$p_{\mathrm{dyn}} = z\frac{\partial}{\partial t}\nabla\cdot(h\overline{\mathbf{u}}) + \frac{z^2}{2}\frac{\partial}{\partial t}\nabla\cdot\overline{\mathbf{u}}, \tag{11}$$

which shows that p_{dyn} is a complex quadratic function of the z coordinate. To simplify the vertical distribution of p_{dyn}, eq. (11) is rewritten as

$$p_{\mathrm{dyn}} = \left\{\frac{(z+h)^2 - D^2}{2} + \tau D[(z+h)-D]\right\}\nabla\cdot\overline{\mathbf{u}}_t. \tag{12}$$

Here we assume that $D\approx h$, which causes negligible difference in the order of $O(\varepsilon\mu^2)$. The dimensionless parameter τ in eq. (12) is expressed as

$$\tau = \frac{\overline{\mathbf{u}}_t\cdot\nabla h}{h\nabla\cdot\overline{\mathbf{u}}_t} \sim \frac{\nabla h}{kh}. \tag{13}$$

Though τ is a variable with respect to time and space, its order can be roughly estimated to be $\nabla h/kh$, which reflects the contribution of water depth variation to wave dispersion. As p_{dyn} mainly exists for short waves in the deep ocean with a smooth bottom, $|\nabla h|$ is much less than kh in most cases where dispersive effects are significant. Thus, and it is reasonable to assume that $\tau\approx 0$. Under this assumption, the vertical distribution of p_{dyn} is approximated to a pure quadratic function of $z+h$ (i.e., vertical distance from the seabed), and the depth-integration of p_{dyn} becomes

$$\begin{aligned}\int_{-h}^{\eta} p_{\mathrm{dyn}}\,\mathrm{d}z &\approx \frac{1}{2}\int_{-h}^{\eta}[(z+h)^2 - D^2]\nabla\cdot\overline{\mathbf{u}}_t\mathrm{d}z\\ &= -\frac{D^3}{3}\nabla\cdot\overline{\mathbf{u}}_t = \frac{2}{3}qD.\end{aligned} \tag{14}$$

Substituting eq. (14) into eq. (9) yields the governing equations of the depth-integrated non-hydrostatic model, that is

$$\begin{cases}\dfrac{\partial\eta}{\partial t} + \nabla\cdot\mathbf{F} = 0,\\ \dfrac{\partial\mathbf{F}}{\partial t} + \nabla\cdot\left(\dfrac{\mathbf{FF}}{D}\right) + gD\nabla\eta\\ +\alpha[D\nabla q + q\nabla(\eta-\beta h)] = 0,\\ \dfrac{\partial W}{\partial t} = \dfrac{q}{D},\end{cases} \tag{15}$$

in which the values of the coefficients α and β are α=2/3, β=0.5. Eq. (15) is almost the same as the conservative form of shallow water equations, except the addition of a vertical momentum equation and the non-hydrostatic pressure in the horizontal momentum equation. In the above derivation, we approximate the complex vertical distribution of p_{dyn} with a simple quadratic function. By doing so, the higher-order derivatives are avoided, and the horizontal momentum equation is significantly simplified.

In previous studies about the depth-integrated non-hydrostatic model, the vertical distribution of p_{dyn} is simply assumed to be linear, which leads to a horizontal momentum equation with α=0.5, β=1.0 (Stelling and Zijlema, 2003; Yamazaki et al., 2009). However, it is shown by the Boussinesq equations that p_{dyn} varies quadratically instead of linearly in the vertical direction. In this paper, we propose a more realistic approximation of the non-hydrostatic pressure (i.e., a pure quadratic function of the vertical distance from seabed), and derive a different horizontal momentum equation with α=2/3, β=0.5. This modification slightly improves the accuracy of the model for smooth bathymetry, and brings it closer to the classical Boussinesq equations.

Tsunamis are simulated in the Cartesian coordinates or the spherical coordinates on Earth surface, so the scalar forms of eq. (15) in both coordinate systems need to be given. In the Cartesian coordinates, the governing equations with the bottom friction effects are written as

$$\begin{cases}\dfrac{\partial\eta}{\partial t} + \dfrac{\partial M}{\partial x} + \dfrac{\partial N}{\partial y} = 0,\\ \dfrac{\partial M}{\partial t} + \dfrac{\partial}{\partial x}\left(\dfrac{M^2}{D}\right) + \dfrac{\partial}{\partial y}\left(\dfrac{MN}{D}\right) + gD\dfrac{\partial\eta}{\partial x}\\ = -\alpha\left[D\dfrac{\partial q}{\partial x} + q\dfrac{\partial(\eta-\beta h)}{\partial x}\right] - f_x,\\ \dfrac{\partial N}{\partial t} + \dfrac{\partial}{\partial x}\left(\dfrac{MN}{D}\right) + \dfrac{\partial}{\partial y}\left(\dfrac{N^2}{D}\right) + gD\dfrac{\partial\eta}{\partial y}\\ = -\alpha\left[D\dfrac{\partial q}{\partial y} + q\dfrac{\partial(\eta-\beta h)}{\partial y}\right] - f_y,\\ \dfrac{\partial W}{\partial t} = \dfrac{q}{D},\end{cases} \tag{16}$$

which (M, N) denote the volume fluxes in the x- and y-directions, and (f_x, f_y) are the bottom friction terms. The

bottom friction is usually evaluated with Manning's empirical formula, which is

$$\begin{cases} f_x = \dfrac{gn^2}{D^{7/3}} M (M^2+N^2)^{1/2}, \\ f_y = \dfrac{gn^2}{D^{7/3}} N (M^2+N^2)^{1/2}, \end{cases} \tag{17}$$

where n is the Manning's roughness coefficient.

When propagating on the surface of Earth, tsunamis are affected by Earth's rotation. In the spherical coordinates defined by the longitude x and the latitude y, the governing equations are expressed as

$$\begin{cases} \dfrac{\partial \eta}{\partial t} + \dfrac{1}{R\cos y}\left[\dfrac{\partial M}{\partial x} + \dfrac{\partial}{\partial y}(N\cos y)\right] = 0, \\ \dfrac{\partial M}{\partial t} + \dfrac{1}{R\cos y}\dfrac{\partial}{\partial x}\left(\dfrac{M^2}{D}\right) + \dfrac{1}{R}\dfrac{\partial}{\partial y}\left(\dfrac{MN}{D}\right) \\ -\dfrac{\sin y}{R\cos y}\dfrac{2MN}{D} + \dfrac{gD}{R\cos y}\dfrac{\partial \eta}{\partial x} \\ = -\alpha\dfrac{1}{R\cos y}\left[D\dfrac{\partial q}{\partial x} + q\dfrac{\partial(\eta-\beta h)}{\partial x}\right] - f_x + 2N\Omega\sin y, \\ \dfrac{\partial N}{\partial t} + \dfrac{1}{R\cos y}\dfrac{\partial}{\partial x}\left(\dfrac{MN}{D}\right) + \dfrac{1}{R}\dfrac{\partial}{\partial y}\left(\dfrac{N^2}{D}\right) \\ +\dfrac{\sin y}{R\cos y}\dfrac{M^2-N^2}{D} + \dfrac{gD}{R}\dfrac{\partial \eta}{\partial y} \\ = -\alpha\dfrac{1}{R}\left[D\dfrac{\partial q}{\partial y} + q\dfrac{\partial(\eta-\beta h)}{\partial y}\right] - f_y - 2M\Omega\sin y, \\ \dfrac{\partial W}{\partial t} = \dfrac{q}{D}, \end{cases} \tag{18}$$

in which R is the radius of Earth, Ω is the angular velocity of Earth's rotation, and the corresponding terms represent the Coriolis forces.

2.2 Numerical methods

As various numerical methods are used in our model for tsunami simulation, here we mainly describe the semi-implicit scheme for solving wave dispersion. The other numerical methods in PCOMCOT are described in detail in Appendix Section S1 (https://link.springer.com), including the moving boundary technique for tsunami inundation, the eddy-viscosity scheme for wave breaking, and the grid nesting algorithm for cross-scale simulation. The variables in the governing equations (eq. (16) or eq. (18)) are discretized in the staggered grid shown in Figure 1, and a semi-implicit finite-difference scheme is adopted to solve the equations. In such method, the shallow water equations are firstly solved explicitly to give an intermediate result. Then, the non-hydrostatic pressure is implicitly solved from a Poisson-type equation. Finally, the shallow water solution is corrected by the non-hydrostatic pressure, and the dispersive solution is obtained.

The explicit scheme for the shallow water equations is similar to the COMCOT model (Liu et al., 1998; Wang, 2009), and the main difference is that we adopt the "flux-centered" scheme proposed by De Almeida et al. (2012) to improve numerical stability. This scheme replaces each flux variable at the previous time step with the weighted average of itself and the two adjacent ones, which introduces slight numerical diffusion without changing the equations to be solved. In model testing, the "flux-centered" scheme effectively eliminates unphysical oscillations near the shore, and the features of tsunami waveforms are unchanged.

To solve the non-hydrostatic pressure q, we express the velocity components as functions of q, and substitute these functions into a rewritten form of the continuity equation, through which an implicit equation of q is constructed. To distinguish between the non-dispersive intermediate result and the final dispersive solution, we use $\widetilde{\mathbf{F}}(\widetilde{M},\widetilde{N})$ and $\widetilde{\mathbf{u}}(\widetilde{u},\widetilde{v})$ to represent the volume flux and depth-averaged horizontal velocity given by the shallow water equations, while $\mathbf{F}(M,N)$ and $\overline{\mathbf{u}}(\overline{u},\overline{v})$ for the dispersive counterparts. According to the horizontal momentum equation in eq. (15), the dispersive flux at the (n+1)-th time step can be expressed as

$$\mathbf{F}^{n+1} = \widetilde{\mathbf{F}}^{n+1} - \alpha\Delta t[D^{n+1}\nabla q + q\nabla(\eta-\beta h)^{n+1}]. \tag{19}$$

Dividing both sides of eq. (19) by the total water depth, the corresponding depth-averaged horizontal velocity is

$$\overline{\mathbf{u}}^{n+1} = \widetilde{\overline{\mathbf{u}}}^{n+1} - \alpha\Delta t\left[\nabla q + q\frac{\nabla(\eta-\beta h)^{n+1}}{D^{n+1}}\right]. \tag{20}$$

Since the vertical velocity varies linearly in the z-direction, w_s, the vertical velocity at the free surface, can be obtained from the vertical momentum equation in eq. (15) as

$$w_s^{n+1} = w_s^n + w_b^n - w_b^{n+1} + \frac{2\Delta t}{D^{n+1}}q, \tag{21}$$

in which w_b is the vertical velocity at the bottom given by eq. (6). By substituting the kinematic boundary conditions (eqs. (5) and (6)) into the continuity equation in eq. (15), and neglecting higher-order dispersive terms, the continuity equation can be rewritten as

$$\nabla\cdot\overline{\mathbf{u}} + \frac{w_s - w_b}{D} = 0. \tag{22}$$

Substituting eqs. (20) and (21) into eq. (22), the Poisson-type equation of q is obtained, that is

$$-\alpha\Delta t\left\{\nabla^2 q + \nabla\cdot\left[q\frac{\nabla(\eta-\beta h)^{n+1}}{D^{n+1}}\right]\right\} + \frac{2\Delta t}{(D^{n+1})^2}$$
$$= -\nabla\cdot\widetilde{\overline{\mathbf{u}}}^{n+1} - \frac{w_s^n + w_b^n - 2w_b^{n+1}}{D^{n+1}}. \tag{23}$$

Discretization of eq. (23) in the staggered grid shown in Figure 1 yields the linear algebraic equation system of q, which is

$$a1_{i,j}q_{i-1,j}+a2_{i,j}q_{i+1,j}+a3_{i,j}q_{i,j-1}+a4_{i,j}q_{i,j+1}+a5_{i,j}q_{i,j}=b_{i,j}. \tag{24}$$

In the Cartesian coordinates, the coefficients and forcing terms in eq. (24) are expressed as

$$\begin{cases} a1_{i,j}=\dfrac{\alpha\Delta t}{(\Delta x)^2}\left(-1+\dfrac{1}{2}\varphi_{i-1,j}\right),\ a2_{i,j}=\dfrac{\alpha\Delta t}{(\Delta x)^2}\left(-1-\dfrac{1}{2}\varphi_{i,j}\right), \\ a3_{i,j}=\dfrac{\alpha\Delta t}{(\Delta y)^2}\left(-1+\dfrac{1}{2}\psi_{i,j-1}\right),\ a4_{i,j}=\dfrac{\alpha\Delta t}{(\Delta y)^2}\left(-1-\dfrac{1}{2}\psi_{i,j}\right), \\ a5_{i,j}=\dfrac{\alpha\Delta t}{(\Delta x)^2}\left[\left(1+\dfrac{1}{2}\varphi_{i-1,j}\right)+\left(1-\dfrac{1}{2}\varphi_{i,j}\right)\right] \\ \quad+\dfrac{\alpha\Delta t}{(\Delta y)^2}\left[\left(1+\dfrac{1}{2}\psi_{i,j-1}\right)+\left(1-\dfrac{1}{2}\psi_{i,j}\right)\right]+\dfrac{2\Delta t}{\left(D_{i,j}^{n+1}\right)^2}, \\ b_{i,j}=-\dfrac{\tilde{u}_{i,j}^{n+1}-\tilde{u}_{i-1,j}^{n+1}}{\Delta x}-\dfrac{\tilde{v}_{i,j}^{n+1}-\tilde{v}_{i,j-1}^{n+1}}{\Delta y}-\dfrac{w_{si,j}^{n}+w_{bi,j}^{n}-2w_{bi,j}^{n+1}}{D_{i,j}^{n+1}}. \end{cases} \tag{25}$$

In the spherical coordinates on Earth surface, these terms are expressed as

$$\begin{cases} a1_{i,j}=\dfrac{\alpha\Delta t}{\left(R\Delta x\cos y_j\right)^2}\left(-1+\dfrac{1}{2}\varphi_{i-1,j}\right), \\ a2_{i,j}=\dfrac{\alpha\Delta t}{\left(R\Delta x\cos y_j\right)^2}\left(-1-\dfrac{1}{2}\varphi_{i,j}\right), \\ a3_{i,j}=\dfrac{\alpha\Delta t\cos y_{j-1/2}}{(R\Delta y)^2\cos y_j}\left(-1+\dfrac{1}{2}\psi_{i,j-1}\right), \\ a4_{i,j}=\dfrac{\alpha\Delta t\cos y_{j+1/2}}{(R\Delta y)^2\cos y_j}\left(-1-\dfrac{1}{2}\psi_{i,j}\right), \\ a5_{i,j}=\dfrac{2\Delta t}{\left(D_{i,j}^{n+1}\right)^2}+\dfrac{\alpha\Delta t}{\left(R\Delta x\cos y_j\right)^2}\left[\left(1+\dfrac{1}{2}\varphi_{i-1,j}\right)+\left(1-\dfrac{1}{2}\varphi_{i,j}\right)\right] \\ \quad+\dfrac{\alpha\Delta t}{(R\Delta y)^2\cos y_j}\left[\left(1+\dfrac{1}{2}\psi_{i,j-1}\right)\cos y_{j-1/2}+\left(1-\dfrac{1}{2}\psi_{i,j}\right)\cos y_{j+1/2}\right], \\ b_{i,j}=-\dfrac{\tilde{u}_{i,j}^{n+1}-\tilde{u}_{i-1,j}^{n+1}}{R\Delta x\cos y_j}-\dfrac{\tilde{v}_{i,j}^{n+1}\cos y_{j+1/2}-\tilde{v}_{i,j-1}^{n+1}\cos y_{j-1/2}}{R\Delta y\cos y_j} \\ \quad-\dfrac{w_{si,j}^{n}+w_{bi,j}^{n}-2w_{bi,j}^{n+1}}{D_{i,j}^{n+1}}. \end{cases} \tag{26}$$

In both the Cartesian and the spherical coordinates, the variables φ and ψ in eqs. (25) and (26) are defined as

$$\begin{cases} \varphi_{i,j}=\dfrac{(\eta-\beta h)_{i+1,j}^{n+1}-(\eta-\beta h)_{i,j}^{n+1}}{D_{i+1/2,j}^{n+1}}, \\ \psi_{i,j}=\dfrac{(\eta-\beta h)_{i,j+1}^{n+1}-(\eta-\beta h)_{i,j}^{n+1}}{D_{i,j+1/2}^{n+1}}. \end{cases} \tag{27}$$

The sparse linear system in eq. (24) is solved iteratively with the Bi-Conjugate Gradient Squared Stabilized (Bi-CGSTAB) method (Van der Vorst, 1992), and the incomplete LU (ILU) preconditioning (Barrett et al., 1994) is used for speeding up the convergence. After the non-hydrostatic pressure q is solved, the vertical velocity at the free surface is calculated from eq. (21), and the dispersive volume flux is obtained by substituting q into eq. (19).

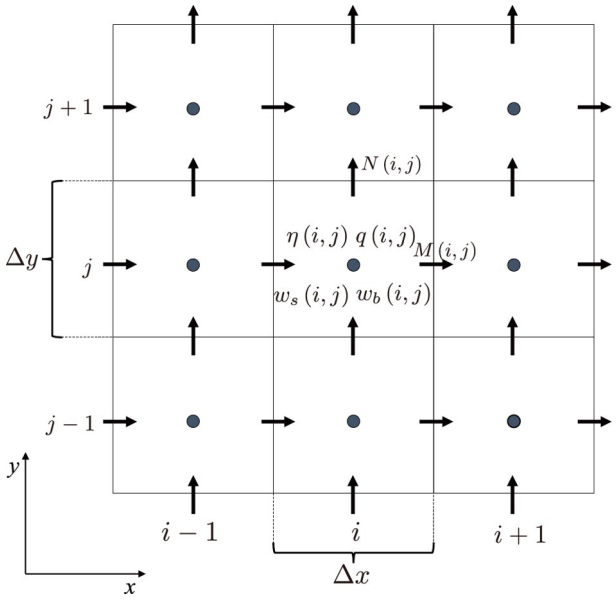

Figure 1 Staggered finite-difference grid used in PCOMCOT. The surface elevation η, non-hydrostatic pressure q, vertical velocity at the surface w_s and that at the seabed w_b are defined at the center of each grid cell, while the volume flux components M and N are defiend at the edges between adjacent cells.

2.3 Computation of solitary wave run-up on a circular island

The propagation, transformation, and inundation of solitary waves around a circular island are influenced by the effects of wave nonlinearity, dispersion, and breaking. Thus, it is challenging to accurately simulate the entire process. The large-scale laboratory experiments of interactions between solitary waves and a circular island were conducted by Briggs et al. (1995). These experiments reveal the fact that, in certain situations, tsunami run-up on the sheltered backside of an island can be comparable or even higher than that on the front side. The collected data have been widely used for validation of tsunami numerical models (e.g., Liu et al., 1995; Chen et al., 2000; Yamazaki et al., 2009).

In the physical experiment, a 62.5 cm-high, 7.2 m toe-diameter, and 2.2 m crest-diameter island, with a 1:4 side slope was installed in a large basin. A directional spectral wave generator was used to produce solitary wave-like profiles. The experiments were carried out at two different water depths (h = 32 cm and 42 cm), and solitary waves with three different wave heights ($\varepsilon = A/h$ = 0.045, 0.096, 0.181) were tested. In this example, we simulate the cases with the water depth of 32 cm, and compare the computed results with the experimental data provided by the National Oceanic

and Atmospheric Administration (NOAA) Center for Tsunami Research. As shown in Figure 2, we place a truncated cone of the same size in the center of a 80 m-long, 24 m-wide computation domain, with 4 m-wide sponge zones applied to both ends in the x-direction. Four gauges are set up to record the water surface elevation, and the locations of these gauges relative to the island are the same as those in the experiment. The coordinates of wave gauges in the numerical model are given in Table 1. In the computation, the grid size is set as $\Delta x = \Delta y = 0.05$ m, and the time step is Δt=0.01 s. The total simulation time is 35 s. A solitary wave profile with the crest at $x = 15$ m is given as the initial condition. The Manning's roughness coefficient is set to be 0.013, corresponding to the smooth concrete surface used in the experiment. As Liu et al. (1995) reported that the waves broke in the laboratory realization, the eddy-viscosity scheme is used to capture wave breaking.

It is observed that for A/h=0.045 and 0.096, the model gives a relatively smooth water surface around the island without significant high-frequency dispersive waves. In the case of A/h=0.181, the surface becomes steep and rough on the back side of the island, and evident short dispersive waves are generated at the collision of the trapped waves from both sides. After that, high-frequency energy is leaking continuously from the trapped waves, forming the mesh-like wave pattern behind the island. Besides, the steep wave profile in the case of A/h=0.181 causes breaking all around the island, reducing the run-up height at the lee side. The waveforms at the four gauges and the inundation around the island are shown in Figure 3. For each case, the measured

Table 1 Coordinates of wave gauges in the numerical model of solitary wave run-up

Gauge number	x (m)	y (m)
6	36.4	0.0
9	37.4	0.0
16	40.0	−2.58
22	42.6	0.0

time series at all gauges are shifted by a uniform time offset, so that the peak arrival time at gauge 6 is the same as the computed value. As seen from Figure 3a, the measured waveforms are well reproduced by the model, except that the amplitude at gauge 22 is overestimated in the A/h=0.181 case. The troughs after the leading crests are slightly underestimated at all gauges, probably due to the numerical dissipation of the upwind scheme for nonlinear terms. In all three cases, the inundation in all directions agree satisfactorily with the measured data (Figure 3b). It is noteworthy that for A/h=0.181, although significant wave dispersion and breaking occurs, the inundation is still accurately predicted by the numerical model. Overall, the good agreement with laboratory data demonstrates the accuracy of the model in computing the propagation, transformation and run-up of dispersive breaking waves.

2.4 Simulation of the 2011 Tohoku earthquake tsunami

To validate our dispersive model and the grid nesting algorithm in a realistic scenario, we simulate the tsunami waves

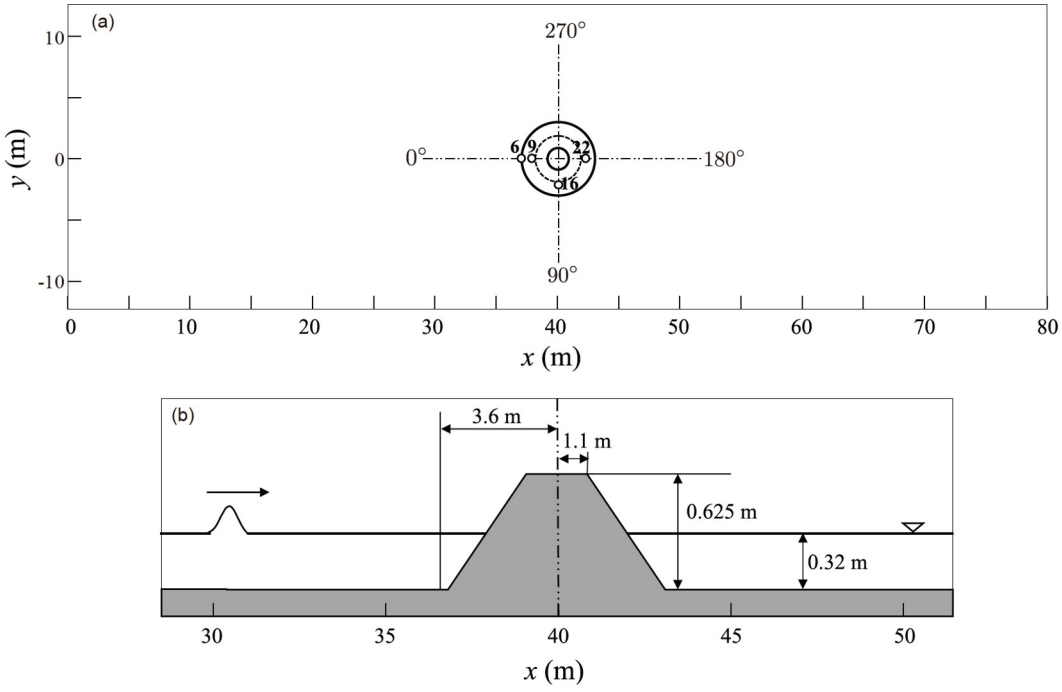

Figure 2 Numerical model of solitary wave run-up on a circular island. (a) and (b) are the top view and side view, respectively. Solid circles in (a) indicate the base and crest of the island, and dashed circle represents the still shoreline. Locations of wave gauges around the island are indicated with hollow dots.

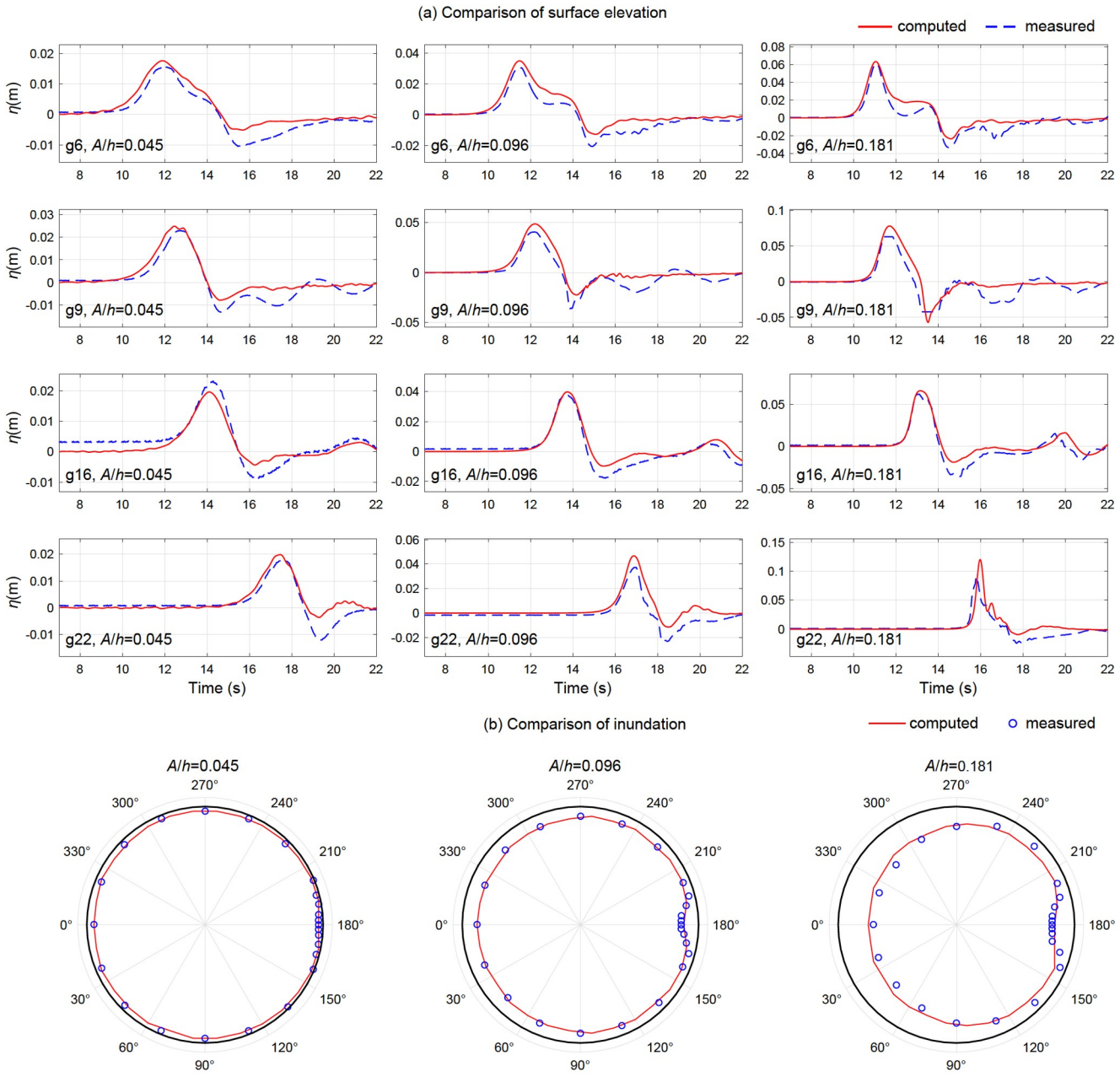

Figure 3 Comparison of (a) water surface elevation and (b) inundation around the circular island given by the numerical model and the experiment. The 0° and 180° directions correspond to the exposed front side and the sheltered back side of the island, respectively.

triggered by the 2011 M_w9.0 Tohoku earthquake. Extensive studies have revealed that large coseismic slip extended to the updip edge of the fault (Fujii et al., 2011; Fujiwara et al., 2011; Satake et al., 2013). The large shallow slip near the trench caused steep ocean bottom deformation, making the dispersive effects of tsunami waves in deep water more pronounced than in most earthquake tsunami events. Many tsunami researchers have suggested the importance of dispersive models for predicting the tsunami waveforms at some Deep-ocean Assessment and Reporting of Tsunamis (DART) stations (e.g., Saito et al., 2011; Glimsdal et al., 2013; Baba et al., 2015).

We obtain the fault geometry from the USGS focal mechanism solution, and estimate a finite-fault source model by inverting the tsunami data based on the linear shallow water equations. The seafloor deformation is calculated using Okada's elastic half-space model (Okada, 1985), and the contribution of horizontal motion to seafloor uplift is considered (Tanioka and Satake, 1996; Hu et al., 2020). The Kajiura filter (Kajiura, 1963; Glimsdal et al., 2013), which calculates the low-pass filtering effect of seawater, is applied to obtain the initial sea surface elevation. Then, two nested grid layers are used to simulate far-field and near-field tsunamis. The outer layer extends from 138°E to 152°E in

longitude, and from 33°N to 44°N in latitude, with a resolution of 1 arc min. The inner layer covers the northeast coast of Japan (140.5°–142.5°E, 37.5°–41°N) at 15-arc sec resolution. The bathymetry data of both layers are extracted from GEBCO2020. Six tsunami stations, including five coastal GPS tide gauges and one DART station in the deep ocean, are used for validation of the computed results. The finite-fault model of the earthquake source, the computational domains and the locations of tsunami stations are displayed in Figure 4a. The total simulation time is 6000 s, and the time steps are set to be 2 s and 1 s for the outer and inner layer, respectively.

As shown in Figure 4b, the tsunami waves propagate seamlessly across the boundary of nested grids, without introducing non-physical oscillations. The snapshots of the outer and inner layer vividly depict how frequency dispersion influences the behavior of tsunami waves in the deep ocean and the shallow water region, respectively. In the deep sea, a series of trailing waves are generated, and both the amplitude and steepness of the leading wave are reduced. On the other hand, when the wavefront approaches the shore and becomes sufficiently steep due to shoaling, dispersion causes splitting of the wave. As a result, the leading wave is amplified, and multiple short-period waves appear near the crest.

To analyze the influence of wave dispersion, we also simulate the tsunami waves using the shallow water equations, and compare both the results of dispersive and non-dispersive models with the tsunami recordings. As seen in Figure 5, The dispersive and non-dispersive models give almost identical results at the coastal gauges, which agree well with the observed waveforms. On the other hand, at the DART station 21418, the dispersive model accurately predicts the amplitude of the leading wave and several trailing waves, while the shallow water model cannot reproduce these features. These results suggest that wave dispersion is important for distant tsunamis triggered by shallow earthquake ruptures, while the shallow water equations are accurate enough for local tsunamis in coastal areas.

In addition to the above examples, we also compute the propagation of solitary wave on a flat bottom and the water surface oscillation in a paraboloidal basin. Good agreement is obtained between the computational results and analytical solutions (Appendix Section S2). The stability and accuracy of our model are satisfactory in both small-scale laboratory scenarios and large-scale realistic scenarios. Furthermore, in parallel implementation on 40 CPU cores, the time cost of the dispersive model is only ~2.5 times longer than the shallow water model, indicating the excellent balance of PCOMCOT between accuracy and efficiency.

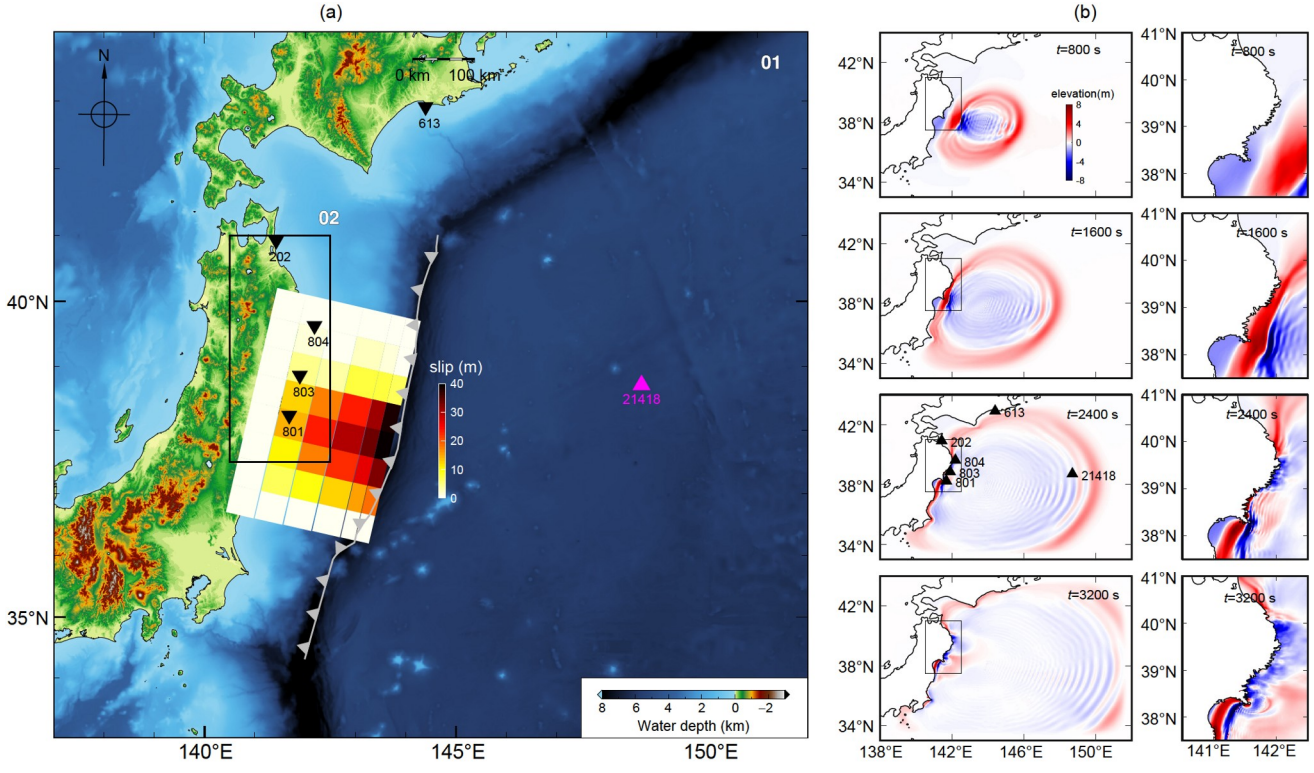

Figure 4 Numerical model and computational results for the 2011 Tohoku earthquake tsunami. (a) The finite-fault source model and the computation domains. The magenta triangle and the black inverted triangles denote the locations of the DART station and the coastal tide gauges, respectively. The rectangular box outlines the domain of the inner grid layer. (b) Snapshots of tsunami wave propagation in the nested grids. The left and right column show the sea surface profiles in the outer and inner layer, respectively.

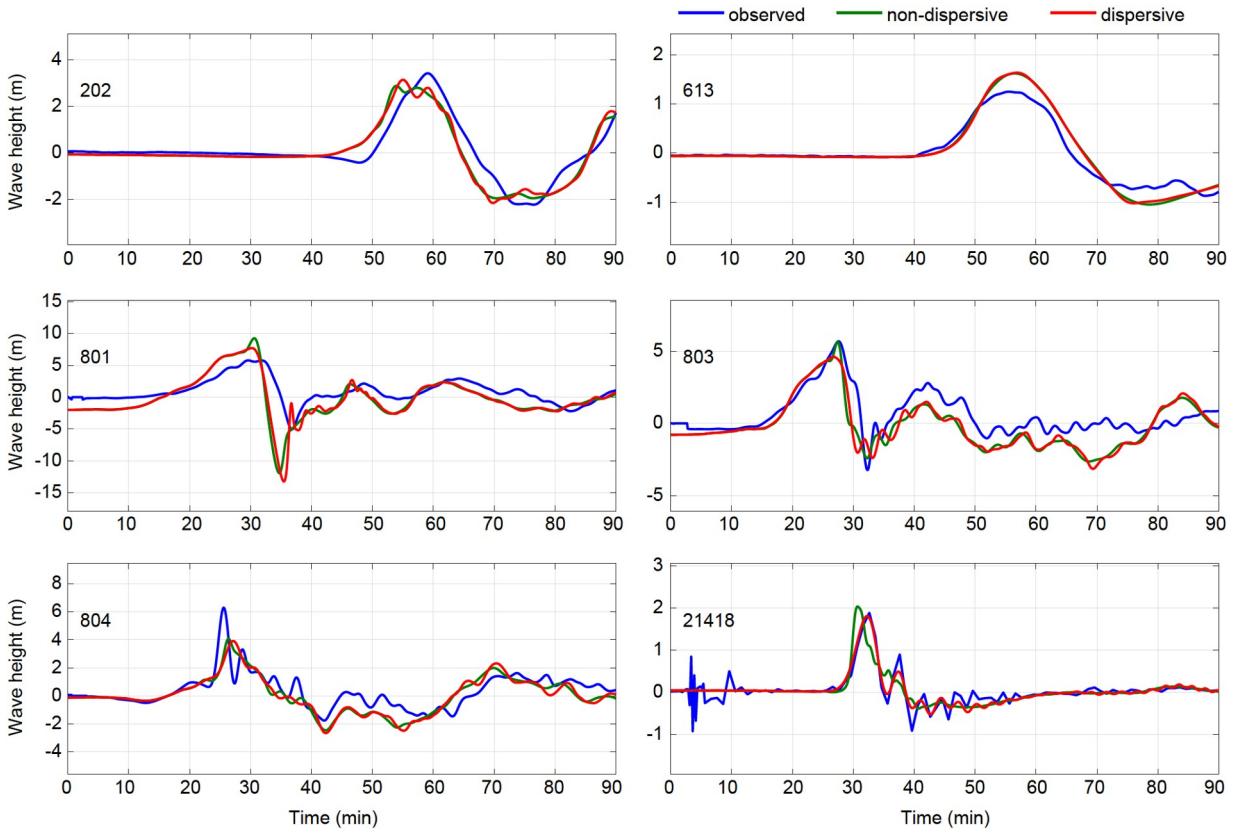

Figure 5 Comparison of computed and observed tsunami waveforms in the 2011 Tohoku earthquake event.

3. Detailed modeling of tsunami hazards in the GBA

In this section, we conduct a detailed tsunami hazard assessment for the GBA under representative earthquake scenarios. Two seismic zones posing the biggest threat to the GBA, i.e., the LFZ and the MSZ, are chosen as the potential tsunami source zones. We start by analyzing the tectonic settings and the corresponding seismogenic mechanisms of the source zones. Then, several representative earthquake source models are proposed based on the results of dynamic rupture simulation, historical records, and interpretations of geodetic data. Large-scale, high-resolution bathymetry models are constructed for the PRD, with special focus on the Hong Kong SAR and Macao SAR. Based on the high-resolution bathymetry data and the PCOMCOT model, we simulate the tsunami waves, currents, and inundation in the GBA induced by the representative earthquakes.

3.1 Representative earthquake source model of the LFZ

As shown in Figure 6, the LFZ extends over 1000 km along the coastline of Southern China, stretching from the Beibu Gulf in the west to the Niushan Island in the east. To the east of the LFZ lies the Philippine subduction zone, and to the west is the Red-River Fault (RRF) system. Thus, the seismogenic mechanisms of the LFZ are mainly controlled by the complex tectonic stress field between these two features. Due to compression from the Philippine subduction zone, the eastern part of the LFZ is under compression-shear stress state (Xu et al., 2006), and is dominated by right-lateral thrust faults, as observed in the 1604 M8.0 Quanzhou earthquake and the 1918 M7.5 Nan'ao earthquake (Peng et al., 2017). In the western part, the RRF system causes tensile-shear stress and seismicity of right-lateral normal faulting, such as the 1605 M7.5 Qiongzhou earthquake (Chen and Huang, 1989).

The segment of the LFZ off the Pearl River Estuary (PRE) is the closet to the GBA, and thus a potential large earthquake in this segment could be the most dangerous to the area of interest. The possible high risk of large earthquakes in this segment is suggested by two facts: (1) The onshore-offshore seismic experiments in the PRE reveal a conjugate fault system at the depth of 10–18 km, where a low velocity zone within the lower crust intersects with the LFZ. Such structure could be related with dynamic nucleation of large earthquakes (Xu et al., 2010; Cao et al., 2014; Cao et al., 2018). (2) The historical seismic activity in this segment is much lower than the eastern and western parts, with no re-

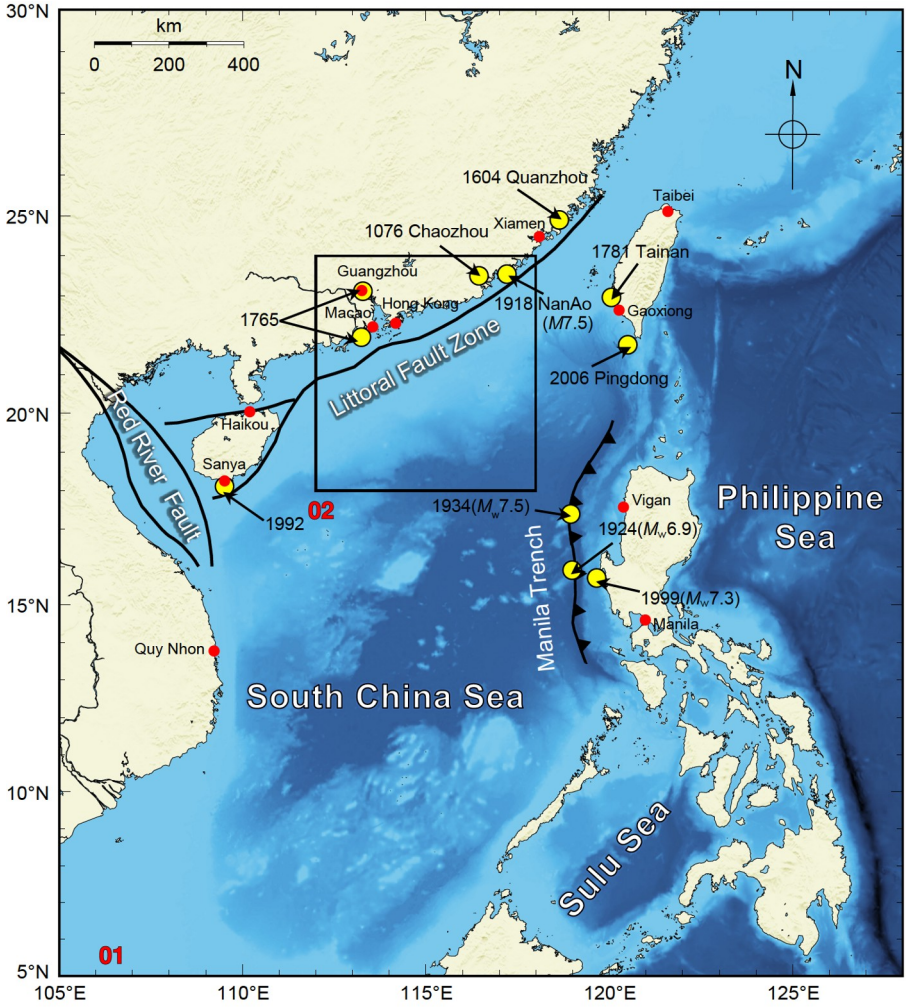

Figure 6 Main tectonic features and historical tsunami records in the SCS. Yellow dots indicate the historical tsunami records in the northeast of SCS (Lau et al., 2010). The locations of the LFZ and RRF are based on the studies of Cao et al. (2014) and Xu et al. (2010), respectively. Red dots are the locations of major cities around the SCS. The rectangular boxes outline the domains of nested grids used in tsunami simulation.

cord of M>6 earthquakes, making it a gap of strong earthquakes (Sun et al., 2012). In addition, because of its intermediate location between the Philippine subduction zone and the RRF system, earthquakes in this segment may very likely contain substantial strike-slip components (Sun et al., 2012). Such inference is supported by the recent microseismic activity in the surrounding area (Chen et al., 2021).

To obtain a reliable earthquake source model for the PRE segment of LFZ, we simulate the spontaneous dynamic rupture process based on the curved-grid finite-difference method (CG-FDM) (Zhang and Chen, 2006; Zhang et al., 2014). This method uses curvilinear grids to construct complex fault models in the presence of surface topography, and the Traction Image method is adopted to accurately implement boundary conditions on the free surface (Zhang and Chen, 2006). Besides, Zhang et al. (2014) introduced the split-node model to treat the discontinuous conditions across the fault, which enables computation of spontaneous rupture on the fault, and has been validated by comparison with the Southern California Earthquake Center (SCEC) benchmarks (Harris et al., 2018). CG-FDM is now an important numerical method for computing spontaneous rupture processes, and has been widely adopted in simulations of real earthquake events (Zhang et al., 2008; Zhang et al., 2019), potential earthquake scenarios (Zhang et al., 2017), and theoretical earthquake models (Hu et al., 2016).

Four elements are generally required to perform dynamic rupture simulation: the fault geometry, the velocity structure around the fault zone, the stress state on the fault surface, and the friction laws describing the relation between frictional strength and fault slip. The fault geometry for the PRE segment of LFZ is provided by Cao et al. (2014) and Wang et al. (2021). As shown in Figure 7a, this part of LFZ consists of three fault segments denoted as F1, F2, and F3 from the west to east, with lengths of around 79, 30, and 55 km, respectively. All the fault segments are southeastward dipping at an angle of 75°, and the width of each segment is ~28 km (Cao et al., 2014). These three fault segments form two step

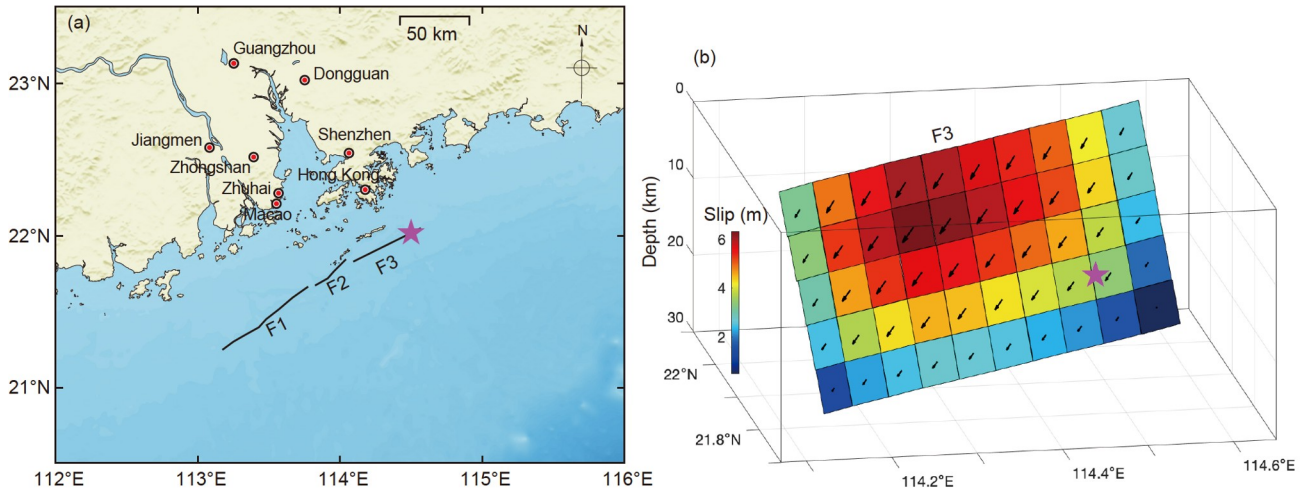

Figure 7 Representative earthquake source model for the LFZ off the PRE. (a) Fault lines of the LFZ off the PRE. (b) M_w7.5 finite-fault model obtained through dynamic rupture simulation. Arrows represent the vectors of coseismic slip, and magenta star indicates the location of nucleation. As rupture is limited to the easternmost F3 segment, only the slip distribution in this segment is displayed here.

overs, which are ~3 km between F1 and F2, and ~4 km between F2 and F3. The velocity structure around the fault zone is obtained from the study of Wang et al. (2021). To determine the stress distribution on the fault planes, we project the triaxial stresses in the surrounding area onto the fault planes. In terms of the principal stresses, $\sigma_V > \sigma_H > \sigma_h$ is set to introduce normal dip-slip components to the simulation result (Anderson, 1951). σ_V is the maximum compressive stress set to be $0.8\rho gh$, σ_H is the intermediate compressive stress ($0.7\sigma_V$), and σ_h is the minimum compressive stress ($0.4\sigma_V$). The relative magnitudes of principal stresses and the direction of the maximum horizontal stress (110°) is estimated based on the stress field in the surrounding area inferred by Kang et al. (2008). In addition, we assume that the maximum compressive stress increases with depth first, and then remain constant below 5 km. The slip-weakening friction law (Ida, 1972) is used to control the slip on the fault plane, where the static and dynamic friction coefficients μ_s and μ_d are set to be 0.38 and 0.23, respectively. The critical slip distance is defined as a function of depth following Zhang et al. (2017). The distributions of initial normal stress, initial shear stress, and dynamic stress drop are displayed in Appendix Figure S6.

In the simulation, the grid size is set to be 100 m to ensure computational accuracy. The initiation of fault rupture is controlled by the nucleation zone, which is a circular region with a radius of 2.5 km located on the fault plane of F3 at the depth of ~18 km (Figure 7b). The initial shear stress within the nucleation zone is slightly (1.005 times) larger than the initial strength of the fault plane. The simulation results indicate that after initiation in the F3 segment, the rupture reaches the western boundary of F3 after 16 s. Impeded by the step overs, once the rupture propagates to the F2 and F1 segments, it can only spread near the surface. This result is consistent with the conclusions of Wesnousky (2006) and Hu et al. (2016) that earthquakes are less likely to jump across step overs above 4 km. Detailed results of our dynamic rupture simulation are provided in Appendix Figure S7. A finite-fault model is obtained by downsampling the slip distribution on the fault plane of F3 segment, which will be used as the input source model for tsunami simulation. As shown in Figure 7b, the rupture area is ~50 km long and ~20 km wide, with an equivalent magnitude of M_w7.5. Controlled by the regional tectonic stress field, the focal mechanism is right-lateral normal faulting with a rake angle of approximately −143°. The maximum slip is ~6 m, occurring at the depth of ~8 km.

3.2 Representative earthquake source models of MSZ

Along the Manila Trench, the Sunda/Eurasian Plate converges obliquely with the Philippine Sea Plate at a rate of ~7 cm/yr (Bautista et al., 2001), making the MSZ one of the fastest subduction zones in the world. Despite the fast convergence rate, large earthquakes are infrequent in the MSZ, with the maximum magnitude of 7.8 in the historical records (Repetti, 1946). An average coupling ratio of ~0.4 is estimated for the MSZ, by inverting a combined dataset of GPS velocities, gravity anomalies, and seafloor bathymetry (Hsu et al., 2012; Hsu et al., 2016). These three characteristics of the MSZ, i.e., the fast convergence rate, lack of large earthquakes, and moderate plate coupling, indicate that the subduction fault is probably accumulating strain energy toward rapid release in a future megathrust event. Because there is transition between the oceanic and continental crust to the south of 14°N and north of 20°N (Yang et al., 1996; Bautista et al., 2001), where the subduction transforms into collision process (Rangin et al., 1988; Kao et al., 2000), we

focus on the middle portion of the MSZ (15°N–19°N) in this study. The middle portion hosted the largest earthquake in history near the Manila Trench (M_w7.5, 1934) (Gutenberg and Richter, 1954; Okal et al., 2011). Using block models constrained by GPS velocities in Luzon and Southern Taiwan, Hsu et al. (2016) inferred that the accumulated strain along the MSZ between 15°N and 19°N in a period of 500–1000 years could be equivalent to an M_w~9.0 earthquake.

Due to the limited spatial-temporal coverage of GPS observations, there is still considerable uncertainty in the interseismic coupling and slip deficit along the MSZ. Therefore, multiple representative earthquake scenarios are defined for tsunami hazard assessment. Assuming a magnitude range between the maximum magnitude in history (M_w7.5) and the maximum potential magnitude (M_w9.0), four earthquake source models of M_w7.5, M_w8.0, M_w8.5, and M_w9.0 are proposed. The epicenter of the M_w7.5 earthquake is set to be the same as that of the largest historical earthquake provided by the USGS catalog. All the other earthquake scenarios occur in the middle portion of the MSZ, and the depth of the rupture is placed as shallow as possible to maximize the tsunami hazards. The focal mechanisms of all the earthquake sources are assumed to be pure thrust. The Slab2.0 model is used to estimate the fault geometry (Hayes et al., 2018). Since the GBA is relatively far from the Manila Trench, tsunami waves at such distance are not sensitive to detailed rupture processes (An et al., 2018; Ren et al., 2022). Therefore, we use uniform slip models to simplify the earthquake sources, and the rupture size is estimated based on the scaling relation of An et al. (2018). By analyzing the similarities among the optimum uniform slip models for the 2011 Tohoku, 2014 Iquique, and 2015 Illapel tsunamis, An et al. (2018) derived the following empirical relation between seismic moment and rupture size:

$$S = 2.89 \times 10^{-11} M_0^{\ 2/3}, \tag{28}$$

in which S is rupture size in km^2, M_0 is seismic moment in N·m, and the ratio of rupture length to width is 1:1. Instead of the entire rupture area, the scaling relation in eq. (28) focuses on the major slip area which plays a leading role in tsunami generation, and thus is more suitable for predicting tsunamis triggered by thrust earthquakes. After the rupture size is estimated, the uniform slip is determined using the definition of seismic moment, $M_0 = \mu \cdot S \cdot \text{slip}$, in which the crustal rigidity μ is assumed to be 40 GPa. The parameters of four representative earthquake sources are given in Table 2. Because an M_w9.0 megathrust earthquake ruptures the entire seismogenic zone in the down-dip direction, its rupture width is limited by the fault size.

3.3 High-resolution bathymetry dataset for the PRD

We construct a high-resolution bathymetry dataset for the PRD based on various independent topo-bathymetry data sources. The dataset includes a 100-m resolution bathymetry model of the PRD, a 25-m resolution model of the entire Hong Kong SAR, and a 10-m resolution model of the Macao SAR. The land elevation data sources for the PRD and Hong Kong include: (1) a 5-m resolution digital terrain model of Hong Kong provided by the Lands Department of Hong Kong SAR; (2) a 1:50,000 topographic map of Hong Kong; (3) the 3-arc sec Shuttle Radar Topography Mission (SRTM) data for covering the PRD. The ocean bathymetry data sources include: (1) dozens of nautical charts covering the coast of Southern China and Hong Kong with scales ranging from 1:4000 to 1:250,000 and (2) the 15-arc sec GEBCO2020 data. The bathymetry model of Macao is provided by Li et al. (2018).

For data correction and integration, the precise locations of shorelines are delineated according to the nautical charts and the topographic map, with the major land reclamation areas under construction extended to their proposed limits. Then, a significant amount of manual process is carried out to remove bridges, elevated roads, etc., from the terrain model to avoid artificial blockages to flood propagation. Furthermore, the elevation of coastal facilities and inland lakes, which are missing from the data sources, are inferred based on the satellite images and street view pictures in Google Earth. Finally, all the corrected and newly added data are uniformly resampled and combined to generate the high-resolution bathymetry models shown in Figure 8. In our bathymetry models of Hong Kong (Figure 8b) and Macao (Figure 8c), the small-scale natural and artificial features such as bays, reefs, ports and dams are clearly recognizable.

To emphasize the importance of high-resolution bathymetry data for tsunami hazard assessment, our newly constructed bathymetry models are compared with GEBCO2020

Table 2 Parameters of representative earthquake source models of the MSZ

Magnitude (M_w)	Epicenter	Depth (km)	Length (km)	Width (km)	Slip (m)
7.5	17.5°N, 119.4°E	4	33	33	5.3
8.0	17.1°N, 119.8°E	12	60	60	8.5
8.5	17.1°N, 120.0°E	19	105	105	16
9.0	17.6°N, 120.0°E	25	300	110	30

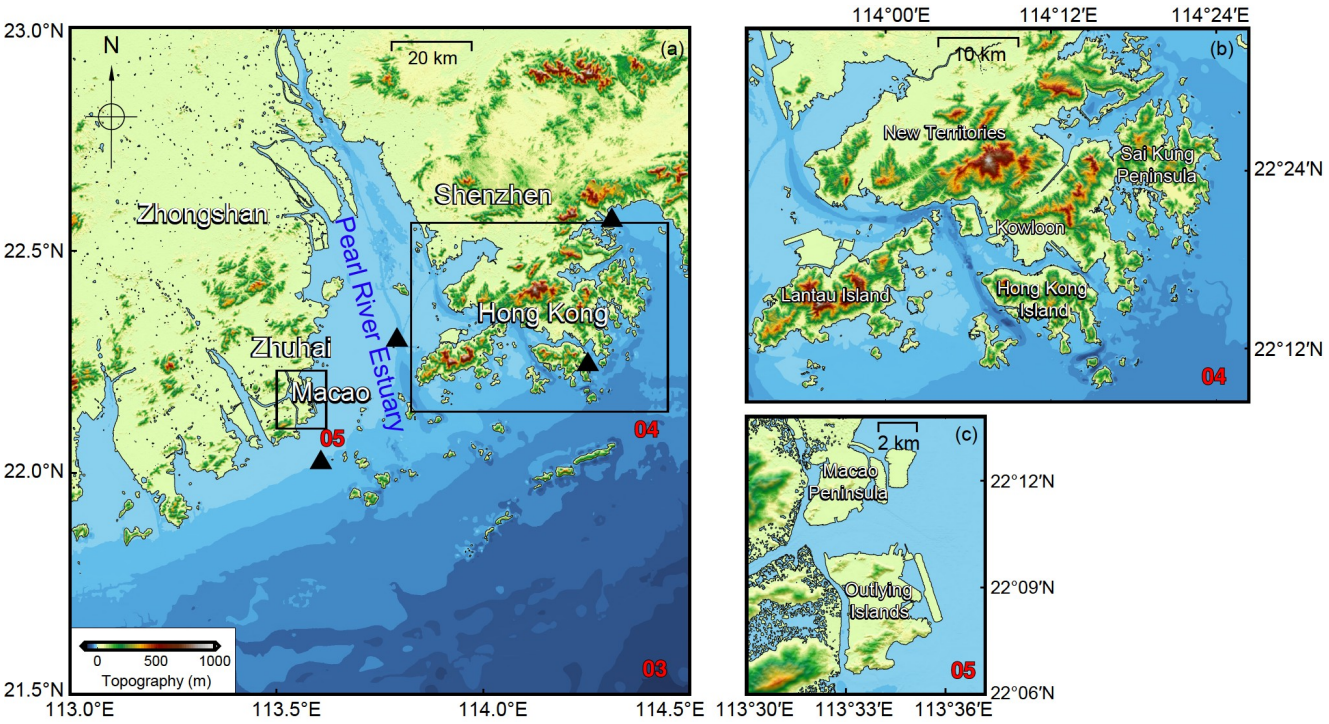

Figure 8 High-resolution bathymetry dataset for the PRD. (a), (b), (c) are the 100-m resolution model of the PRD, the 25-m resolution model of Hong Kong, and the 10-m resolution model of Macao, respectively. Black triangles in (a) denote the virtual gauges used to record tsunami waves, which are in southern offshore of Macao, PRE, eastern offshore of the Hong Kong Island, and Mirs Bay, from the west to east.

for two local areas in Hong Kong—the Victoria Harbour and the bay to the southwest of Sai Kung Peninsula. As seen in Figure 9, both areas have highly complex topography. The water channel of the Victoria Harbour has sudden expansions and contractions, with many piers and ports on both sides. The bay to the southwest of Sai Kung Peninsula is dotted with islands of varying sizes, forming narrow channels, and a large number of coves are distributed along the coastline. None of these features are resolved in GEBCO2020. For example, the southeastern entrance to Victoria Harbour is filled with land in GEBCO2020, so tsunamis would be blocked out if GEBCO2020 is used for tsunami simulation. In brief, large-scale and high-resolution bathymetry data where shorelines and coastal facilities can be clearly recognized, are essential for accurate modeling of tsunami hazards in the GBA.

3.4 Tsunami simulation

The high-resolution bathymetry models are nested into the part of GEBCO2020 data covering the SCS, forming a system of nested grids. The PCOMCOT model is applied to simulate the tsunami hazards induced by the representative earthquakes in the MSZ and LFZ. After an earthquake occurs, coseismic rupture propagates outward from the hypocenter at a finite speed, causing different parts of the fault surface to rupture at different moments. Since the rupture velocity (~2 km/s) is much faster than that of tsunami waves (typically ~0.2 km/s), the rupture duration is usually much shorter than tsunami periods. So, the effects of kinematic rupture process on tsunami generation are negligible in most cases. For example, Satake et al. (2013) proposed a kinematic source with a rise time of up to 2 min for the 2011 M_w9.0 Tohoku earthquake through tsunami data inversion. It was found that the tsunami waveforms generated by the kinematic source are similar to those by the instant rupture model, with just a slight delay in arrival time. In some extreme cases, such as the 2004 M_w9.3 Sumatra earthquake, where the rupture extended over 1000 km along the trench, the kinematic rupture process may have significant influence on tsunami waves (Fujii and Satake, 2007; Williamson et al., 2019). In this study, the representative earthquake sources in the LFZ and MSZ have relatively short rupture durations, so the rupture can be treated as instantaneous. A comparison of tsunami waves generated by instant and kinematic rupture sources in the LFZ and MSZ is presented in Appendix Section S3. The coseismic seafloor deformation is calculated using Okada's elastic half-space model (Okada, 1985). Under the assumptions of shallow water and instantaneous rupture, the initial sea surface elevation is equal to the vertical seafloor displacement plus the contribution of horizontal motion (Tanioka and Satake, 1996).

As tsunami waves show different physical characteristics

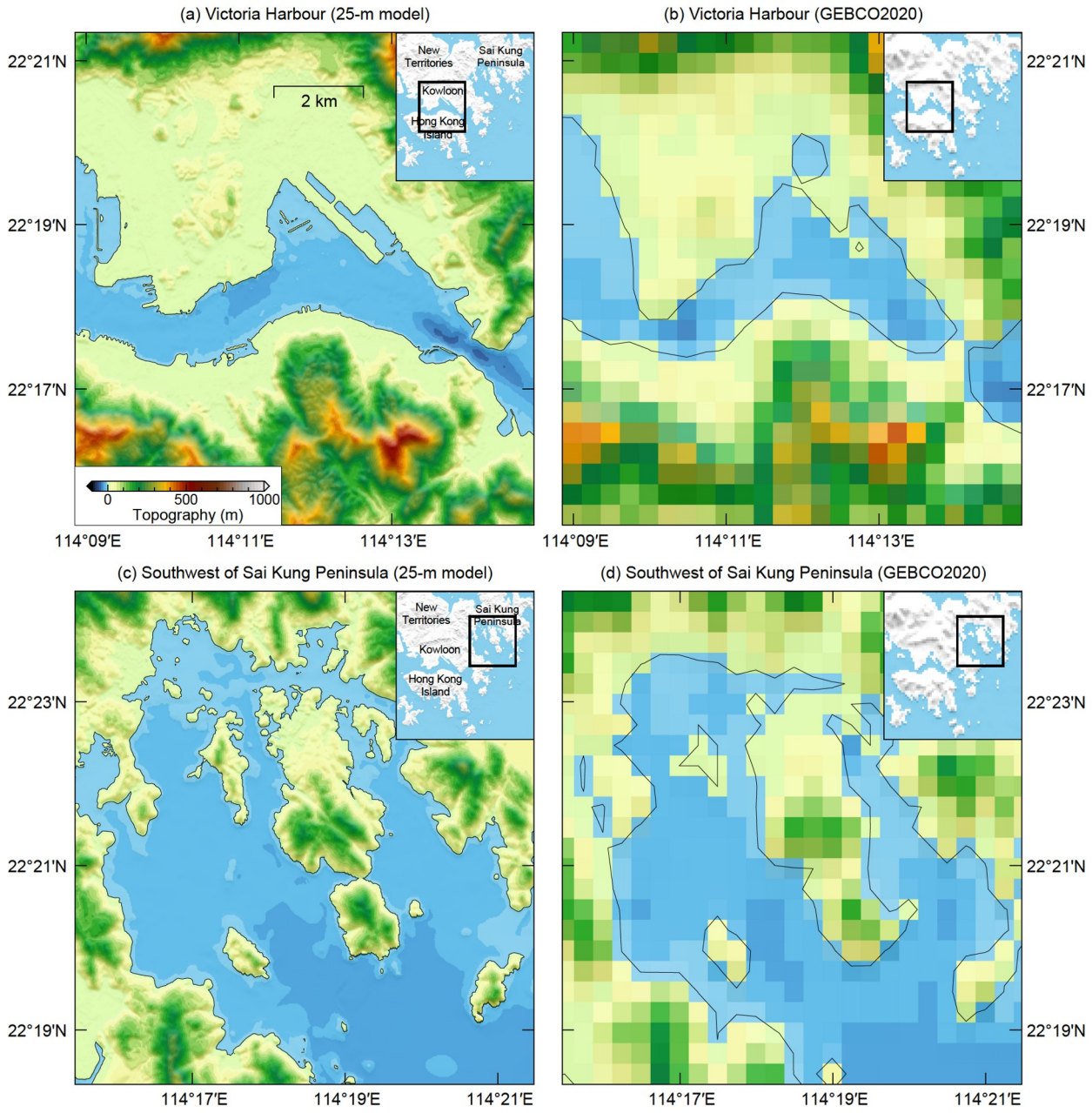

Figure 9 Comparison of the high-resolution bathymetry model of Hong Kong and the GEBCO2020 data. Small panel on the right top of each subfigure denotes the location of the compared area in the corresponding model.

in the deep ocean and the coastal area, different tsunami models are solved in the nested grids to enhance computational efficiency and stability. In the SCS basin, tsunamis behave as linear waves, and the short-wavelength components may be affected by frequency dispersion. Therefore, the linear dispersive model is used to calculate tsunami propagation in the SCS. In the coastal zone, tsunamis are nonlinear shallow waves, and the steep wavefronts may break, so the nonlinear shallow water equations are solved with wave breaking captured by the eddy-viscosity scheme. A total of five grid layers, with nesting levels up to 4, are used in our simulations. The outermost layer covers the entire SCS shown in Figure 6, while the innermost layers correspond to the high-resolution bathymetry models of Hong Kong (Figure 8b) and Macao (Figure 8c). Table 3 lists the basic parameters of the nested grids and the tsunami model solved in each layer. The duration time of simulation is 25,000 s, and the Manning's coefficient for bottom friction is set as 0.03. Four virtual gauges are set up to record the tsunami waves in the PRE, the southern offshore of Macao, the eastern offshore of Hong Kong Island, and the Mirs Bay. All gauges are located on the 10-m isobath.

Table 3 Parameters of nested grids and the tsunami model solved in each layer

Layer ID	Domain	Resolution	Tsunami model
01	SCS (Figure 6)	1 arc min	linear, dispersive
02	Northern SCS (Figure 6)	15 arc sec	nonlinear, dispersive
03	PRD (Figure 8a)	3 arc sec (100 m)	nonlinear, dispersive
04	Hong Kong (Figure 8b)	0.8 arc sec (25 m)	nonlinear, breaking
05	Macao (Figure 8c)	0.33 arc sec (10 m)	nonlinear, breaking

4. Result analysis and tsunami hazard assessment

4.1 Characteristics of tsunami waves induced by the M_w7.5 LFZ earthquake

The sea surface deformation and tsunami waves induced by the M_w7.5 LFZ earthquake off the PRE are displayed in Figure 10. As shown in Figure 10a, the right-lateral normal-faulting earthquake causes coseismic uplift on the nearshore side and subsidence on the offshore side. The maximum uplift and subsidence are approximately 1.5 m and −2.5 m, respectively. As the direction of tsunami propagation is nearly perpendicular to the fault strike and the earthquake source is close to the coastline, the tsunami energy mainly impacts the Hong Kong SAR, which is directly facing the earthquake source. As seen in Figure 10b, the tsunami waves are higher than 0.5 m in the southeastern coast of Hong Kong, reaching to the maximum of ~1 m in several bays and narrow channels. The tsunami waves decease rapidly to the west and east of Hong Kong, with a maximum height of ~0.3 m in Macao and the Mirs Bay.

For potential LFZ earthquakes off the PRE, special attention should be given to the hazards from negative tsunami waves. As the initial subsidence is larger than the uplift and occurs in the area with deeper water, the resulting negative waves could be more dangerous. As shown in Figure 10c, compared to the positive waves, the energy of negative waves is more concentrated on the coastline of Hong Kong. The maximum negative waves in the southeastern coast of Hong Kong are lower than −1 m, reaching −2 m in some small bays. The rapid subsidence of seawater could lead to grounding of vessels in the harbors and huge losses in marine fisheries. Thus, effective measures need to be taken in the GBA to reduce the potential hazards from negative tsunami waves.

The special topography around the PRE has strong influence on the propagation of tsunami waves, leading to the complex tsunami waveforms shown in Figure 10d. After the leading crest and trough, each location is impacted by multiple waves of comparable heights. Moreover, the sea surface around Hong Kong experiences persistent large oscillations. These phenomena are closely related with the effects of the Dangan Islands, the coastlines, and the continental slope on tsunami waves. Because the Dangan Islands are located right in front of the earthquake source, part of tsunami waves diffracts around the islands. The direct waves, and the diffracted waves from both sides of the islands, together cause a leading crest of ~0.5 m and a trough of about −2 m near the Hong Kong Island. Then, the tsunami waves reflect back and forth between the coastline of Hong Kong and the Dangan Islands, leading to the subsequent oscillations. Some trapped waves behind the Dangan Islands radiate in the offshore direction through the gaps between the islands. Due to the rapid increase in water depth, these waves are refracted eastward and westward, forming the second peak and trough in Macao. Additionally, tsunami waves reflected from the eastern side of the PRE could also affect the surrounding areas. For example, the highest wave crests in the southern offshore of Macao and the Mirs Bay (both ~0.2 m) are actually reflected waves from the Lantau Island and the Sai Kung Peninsula in Hong Kong, respectively.

4.2 Characteristics of tsunami waves induced by representative MSZ earthquakes

The sea surface elevation and tsunami wave height induced by representative MSZ earthquakes (M_w7.5–9.0) are displayed in Figure 11. The M_w7.5, M_w8.0, M_w8.5, and M_w9.0 earthquakes cause maximum sea surface uplifts of approximately 2, 3, 6, and 12 m, respectively (Figure 11a–11d). Because the coseismic rupture extends to the up-dip edge of the fault, steep sea surface deformation similar to that caused by the 2011 Tohoku earthquake appears near the trench, resulting in short-wavelength components of tsunami waves.

The tsunamis generated by MSZ earthquakes arrive in the Hong Kong Island ~3 h later, and enters the PRE ~3.5 h later. The M_w7.5, M_w8.0, M_w8.5, and M_w9.0 earthquakes induce tsunami waves of approximately 5 cm, 0.5 m, 1.5 m, and 6 m in the PRE, respectively (Figure 11e–11h). Due to the refraction caused by the topography of the northern SCS, tsunami energy around the PRE is directed towards the west. Comparison of Figure 11e–11h reveals that the tsunami waves induced by the M_w7.5 MSZ earthquakes are almost completely focused on the western side of PRE. Nonetheless, with increase in magnitude, the impacts on both sides be-

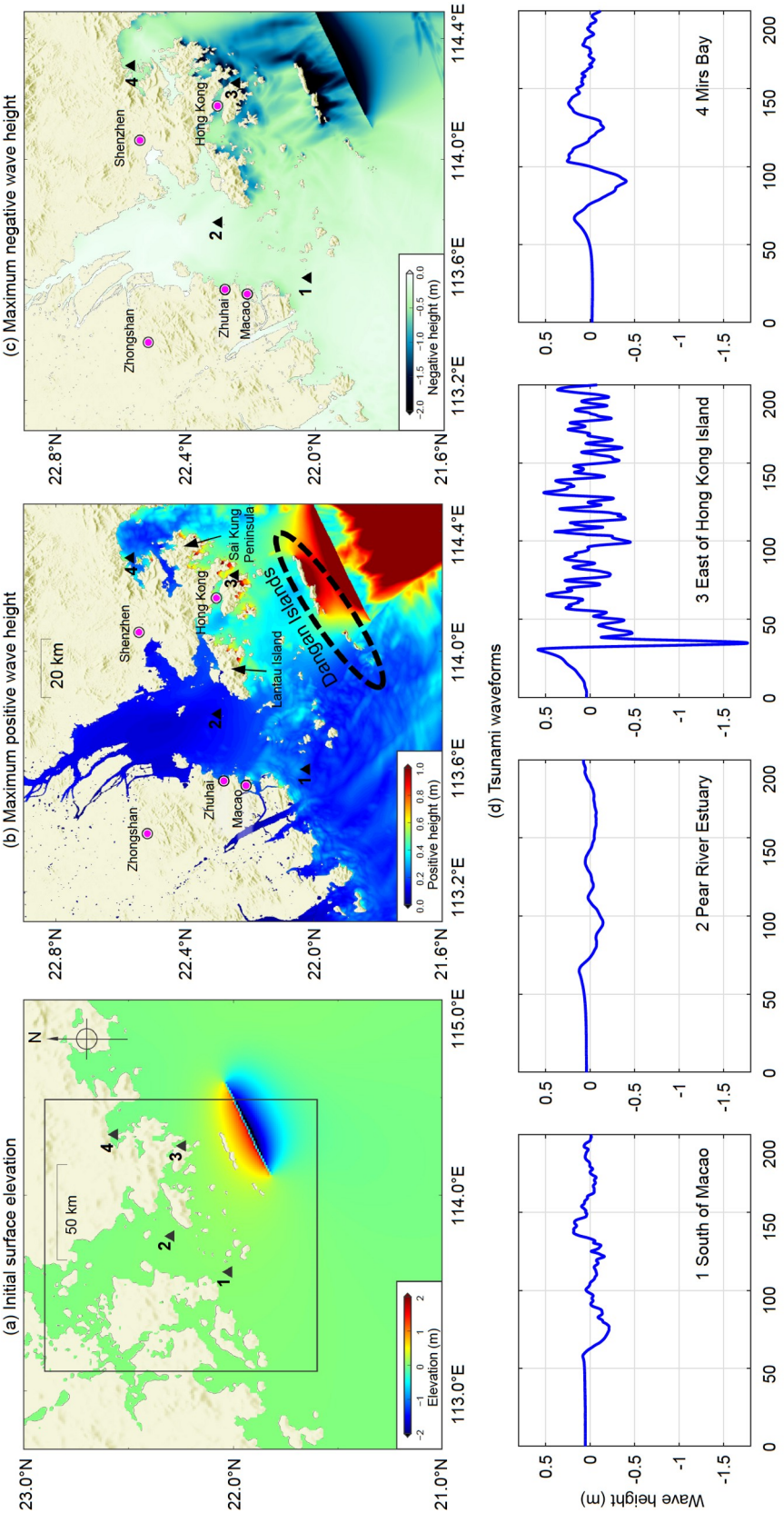

Figure 10 Sea surface deformation and tsunami waves generated by the M_w7.5 LFZ earthquake off the PRE. Rectangular box in (a) indicates the smaller region plotted in (b) and (c). Black triangles denote the locations where tsunami waves are recorded, and the name of each location is given in (d).

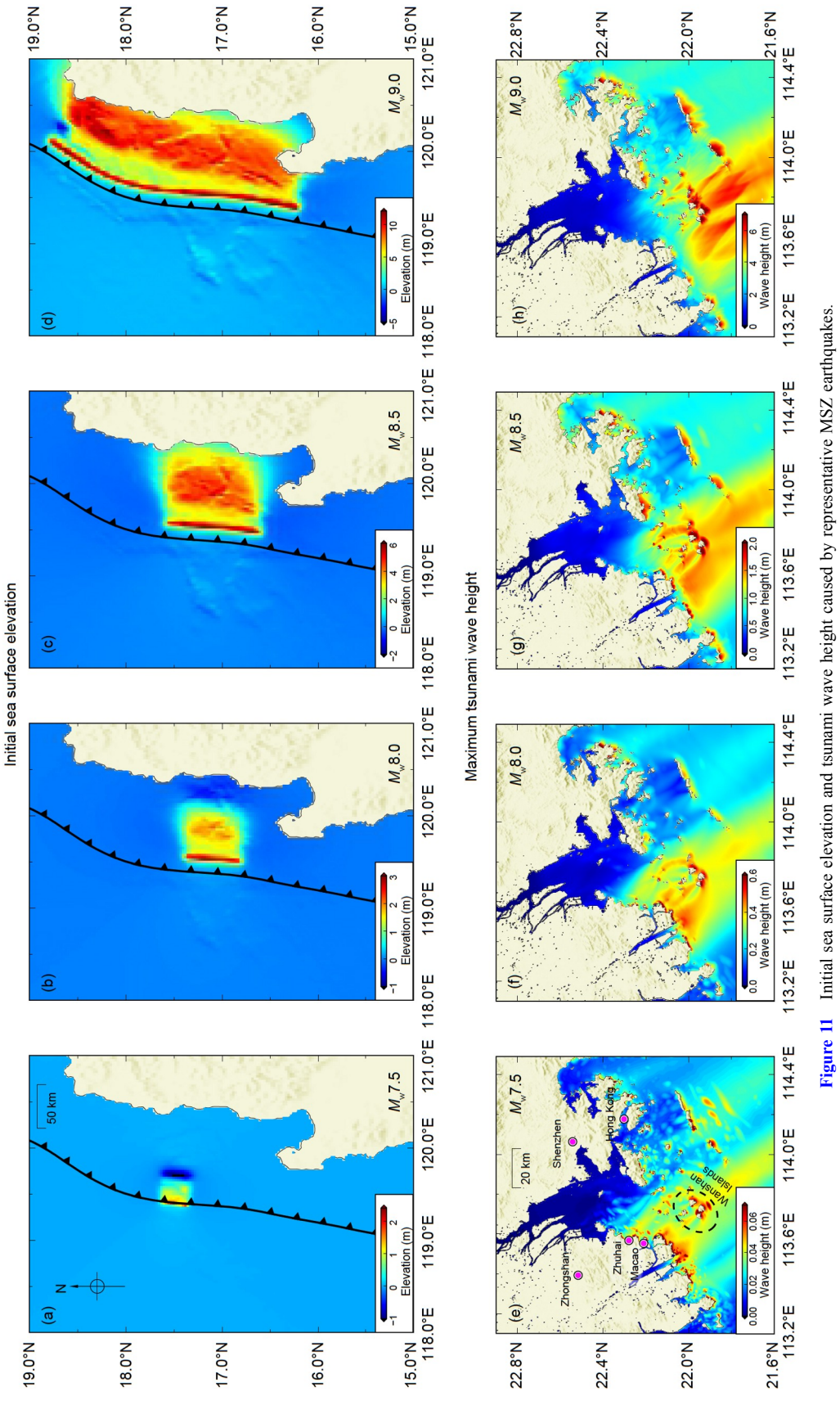

Figure 11 Initial sea surface elevation and tsunami wave height caused by representative MSZ earthquakes.

come more and more comparable. This can be explained with the tsunami radiation patterns and the local topography. On one hand, tsunami energy initially radiates in the direction perpendicular to the trench. When far-field tsunamis reach the shore, they would impact the coastline at nearly normal incidence due to the strong refraction at the continental break. As the rupture length of an M_w9.0 earthquake is much longer than that of an M_w7.5 earthquake, the tsunami waves generated by an M_w9.0 megathrust event would impact a broader area along the coastline. On the other hand, tsunami waves generated by moderate earthquakes have shorter wavelengths, and are more likely to directly pass through the gaps between the Wanshan Islands on the western side of PRE (Figure 11e). In contrast, the longer waves generated by megathrust earthquakes undergo strong diffraction when passing through these islands. As a result, the energy reaching the coastline behind these islands is dispersed.

4.3 Tsunami inundation hazards from great MSZ earthquakes

As tsunamis triggered by representative LFZ earthquakes and M_w~8.0 MSZ earthquakes could hardly inundate the land in the GBA, here we focus on the potential inundation hazards from the M_w9.0 MSZ megathrust event. The computational results indicate that in the Macao SAR, tsunami inundation mainly occurs on the outlying islands. Although the coastline of Macao Peninsula is impacted by the tsunami waves, the extent of inland inundation is quite limited. As shown in Figure 12a, in the M_w9.0 MSZ megathrust event, the maximum inundation depth on the outlying islands of Macao is up to ~5 m, occurring at the southernmost tip of Coloane (i.e., the Hac Sa Beach). The inundation distance at the Hac Sa Beach is ~200 m. Besides, the eastern coast of Cotai undergoes moderate inundation, with a depth of ~1 m.

Compared with the Macao SAR, the Hong Kong SAR has a much larger land area and more complicated coastal topography. Tsunami inundation in Hong Kong would primarily occur in the ports and bays on the southeastern coast. These locations are directly facing the incident tsunami waves, and the semi-enclosed coastal structures prevent the leaking of tsunami energy. In contrast, tsunami impacts on the northwestern coast are relatively moderate. The Tai Long Wan, on the southeastern tip of Sai Kung Peninsula, is the most susceptible to tsunami inundation in Hong Kong. In the M_w9.0 MSZ megathrust event, the inundation depth and distance at this location reach up to ~6 m and ~400 m, respectively. In addition to the suburban areas like the Tai Long Wan, the urban areas along the shorelines between the Hong Kong Island and the Kowloon Peninsula, are also significantly inundated. Despite the smaller inundation extent, the dense population and infrastructure in these areas could lead to much heavier property damage and casualties. Therefore, more attention should be paid to these areas when considering potential inundation hazards in the Hong Kong SAR.

The distribution of inundation along the ~10 km-long water channel between the Hong Kong Island and the Kowloon Peninsula, caused by the M_w9.0 MSZ earthquake, is depicted in Figure 12b–12d. The depicted area is centered at the Victoria Harbour, with the Junk Bay and Chai Wan to the southeast and the Kwai Tsing Container Terminals to the northwest. As shown in Figure 12b, severe inundation occurs at the Junk Bay and Chai Wan. On the east of Junk Bay and around the Chai Wan, the tsunami reaches a distance of >300 m inland, with a maximum inundation depth of ~2 m. The Chai Wan breakwater fails to stop huge tsunamis generated by MSZ megathrust earthquakes. The severe inundation at the Junk Bay and Chai Wan is closely related to the geographical location and the local topography. To the southeast, this area is connected with the broader Tathong Channel. While to the northwest, the outlet narrows suddenly due to the presence of mountains. When tsunamis enter this area from the southeast, the waves become higher due to contraction of the channel, and then could hardly pass through the narrow outlet. Beside the inundation hazards, this enclosed area is prone to undergo serious harbor oscillations. Thus, the Junk Bay and the Chai Wan should be one of the top priorities of investments in tsunami mitigation and preparedness in Hong Kong.

Along the shorelines of Victoria Harbour (Figure 12c), there are relatively narrow inundation zones with depths between 1–2 m, and most piers are flooded. Although the inundation distance seems limited, the businesses, transportation facilities, and the residences close to the shorelines could be seriously damaged. To the northwest of Victoria Harbour, the Kwai Tsing Container Terminals (Figure 12d) undergoes moderate inundation at its southern end, caused by the tsunami waves coming from the PRE. Considering that the Kwai Tsing Terminals is one of the most crucial port facilities in Hong Kong, ranking eighth globally in container throughput, inundation at this location could significantly impact the trade in East and Southeast Asia.

Compared to the M_w9.0 megathrust earthquake, the M_w8.5 MSZ earthquake induces relatively minor inundation in the GBA (Figure 12e–12h). Along the coasts of Hong Kong and Macao, the inundation depths are mostly lower than 1 m, and the flooded areas are small. So, risk assessments for onshore facilities should focus on the largest potential earthquakes in the MSZ, and build detailed inundation maps under extreme scenarios.

4.4 Tsunami current hazards from LFZ and MSZ earthquakes

Tsunami disasters are not limited to sea surface oscillations

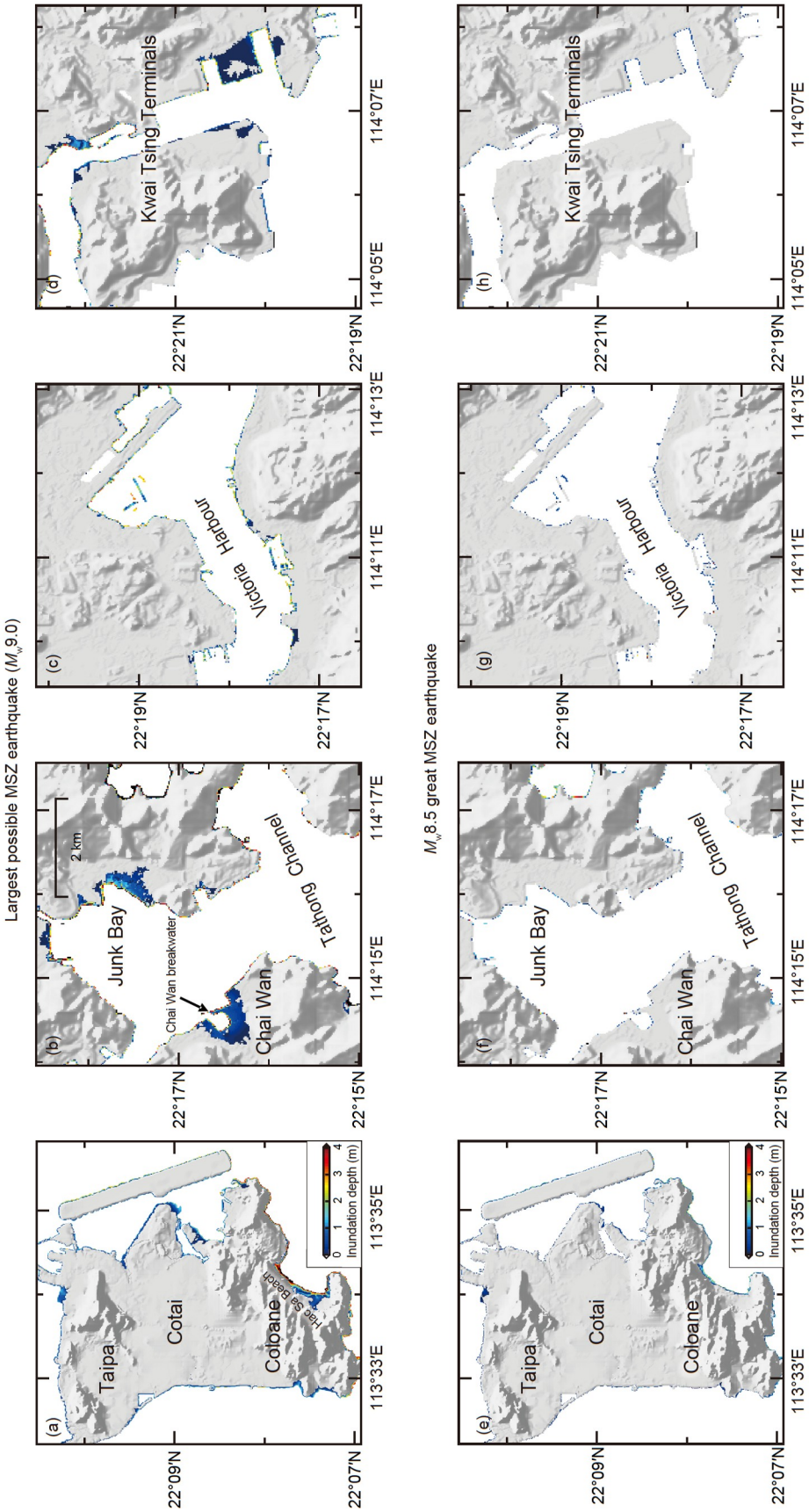

Figure 12 Tsunami inundation maps for severely impacted areas in Macao and Hong Kong, caused by MSZ megathrust earthquakes. (a) and (e) are the outlying islands of Macao; (b) and (f) are the Junk Bay and Chai Wan, Hong Kong; (c) and (g) are the Victoria Harbour, Hong Kong; (d) and (h) are the Kwai Tsing Container Terminals, Hong Kong.

and coastal inundation. The powerful tsunami currents can be highly destructive to maritime facilities (Lynett et al., 2014; Wang et al., 2016). In earthquake tsunami events, even if the tsunamis cause no flooding in far-field areas, the tsunami currents could be strong enough to destroy docks and terminals (Borrero et al., 2013; Lynett et al., 2013; Wilson et al., 2013). Additionally, localized high-speed flows can easily break the mooring lines securing vessels and pull them out of terminals, leading to serious accidents (Okal et al., 2006a, 2006b). Despite the large number of destructive events caused by tsunami currents, the potential hazards from strong currents still remainunderappreciated in tsunami hazard assessments around the SCS. As nearshore tsunami currents are governed by nonlinear physics and have much larger spatial and temporal variability than tsunami waves, reliable tsunami current modeling is highly challenging. In this study, the refined hydrodynamic model we build allows us to perform reasonably accurate simulations of tsunami currents in the GBA.

For all the representative earthquake scenarios considered in this paper, the distribution patterns of tsunami currents are similar, with the local maximum current velocities occurring in the narrow water bodies directly facing the incident tsunamis. As shown in Figure 13, the Macao SAR (left), the Victoria Harbour (middle), and the bay to the southwest of Sai Kung Peninsula (right) in Hong Kong, are chosen to show the detailed distributions of tsunami currents. The Victoria Harbour has a long narrow channel with numerous costal facilities along the shorelines, and thus may be the most vulnerable to tsunami currents. The bay to the southwest of Sai Kung Peninsula is the place with the strongest tsunami currents in Hong Kong.

The tsunami currents in the above three areas, induced by the M_w7.5 LFZ earthquake off the PRE, are presented in Figure 13a–13c. The tsunami currents in Macao are relatively mild (Figure 13a), exceeding 1.5 m/s only in the narrowest areas between the southwestern end of Coloane and the Great Hengqin Island, as well as between the airport and Coloane. In Hong Kong, extensive tsunami currents of ~1.5 m/s occur in the Victoria Harbour (Figure 13b), with the maximum speed reaching 2 m/s at the southeastern entrance. In the bay to the southwest of Sai Kung Peninsula (Figure 13c), slightly destructive currents of ~3 m/s appear between Kau Sai Chau and the Sai Kung Peninsula, as well as between the small islands in the Inner Port Shelter.

As the tsunami current speeds induced by the M_w8.0 MSZ earthquake are less than 1 m/s in most areas of the PRD, only the tsunami current hazards from the M_w9.0 and M_w8.5 MSZ earthquakes are discussed here. As shown in Figure 13d, in the M_w9.0 MSZ megathrust event, the outlying islands of Macao are impacted by extensive tsunami currents of 2–3 m/s from the east. In the narrowest areas mentioned above, the maximum current speed reaches up to 6 m/s. Strong currents with speed of >2.5 m/s occur throughout the Victoria Harbour (Figure 13e), and the local speed suddenly rises to 5 m/s at the southeastern entrance. In the bay to the southwest of Sai Kung Peninsula (Figure 13f), the maximum current speeds in many narrow waterways exceed 5 m/s. Between Kau Sai Chau and the Sai Kung Peninsula, the entire ~10 km waterway from the Rocky Harbour to Tsam Chuk Wan are swept by powerful tsunami currents. The tsunami currents in Hong Kong induced by the M_w8.5 MSZ earthquake are comparable to that by the M_w7.5 LFZ earthquake (Figure 13h, 13i). In Macao, the M_w8.5 MSZ earthquake could also induce extensive dangerous currents to the east of the outlying islands (Figure 13g).

According to the relationship between tsunami current speed and harbor damage compiled by Lynett et al. (2014), there is a threshold for damage initiation at 1.5 m/s, and the damage transitions from moderate to major when 3 m/s is exceeded. Tsunami currents of >4.5 m/s could cause extreme damage in historical events, where over 50% of docks and vessels were damaged. Therefore, an M_w7.5 LFZ earthquake could cause minor damage at several locations and affect maritime transportation in the near-field area. An M_w9.0 MSZ megathrust earthquake is capable of generating catastrophic tsunami currents in the GBA, causing extreme damage to coastal facilities and vessels, and disrupting maritime activities across the entire region. By comparing the tsunami currents and coastal inundation induced by the M_w9.0 MSZ earthquake, we observe a considerable discrepancy between the spatial distributions of current and inundation hazards. For example, the extent of tsunami inundation on the outlying islands of Macao and in the Victoria Harbour (Hong Kong) seem to be relatively limited. However, these areas are actually severely impacted by localized high-speed tsunami currents. Such discrepancy indicates that a tsunami hazard assessment result without considering the risk of tsunami currents may be incomplete, especially when it is used to make mitigation strategies or evaluate the potential losses.

4.5 Influence of wave dispersion on tsunami hazards

To assess the influence of wave dispersion on potential tsunami hazards in the GBA, we calculate the tsunami waves using the shallow water equations. Both the dispersive and non-dispersive simulations are performed in the same nested grids. The tsunami waveforms given by dispersive and non-dispersive models are plotted in Figure 14. The M_w7.5 LFZ earthquake involves a small rupture size and oblique-slip motion, which leads to short-wavelength components of tsunami waves. However, the computed waveforms show that because the source area is near the coastline and the

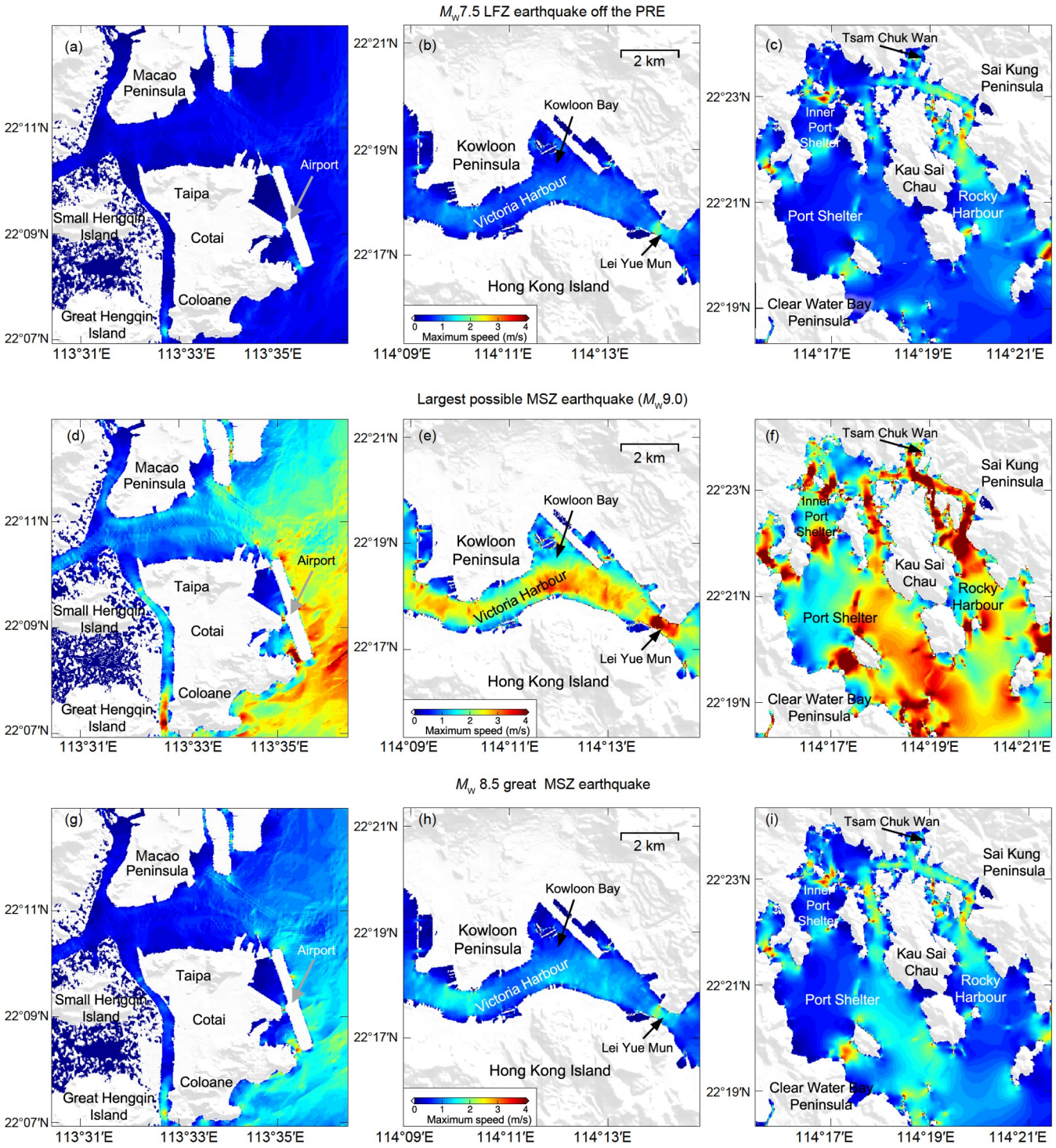

Figure 13 Tsunami currents in Macao and Hong Kong, caused by representative LFZ and MSZ earthquakes. The left, middle, and right columns are for Macao, the Victoria Harbour (Hong Kong), and the bay to the southwest of Sai Kung Peninsula (Hong Kong).

water depth along the tsunami propagation path is as shallow as ~100 m, the dispersive effects are negligible. This is similar to the tsunami from the 2018 collapse of Anak Krakatau volcano. Despite that the tsunami source was only a few kilometers in size, little wave dispersion was observed because of the shallow water in the Sunda Straits (Zhu et al., 2021). As for the tsunami triggered by the M_w7.5 MSZ earthquake, frequency dispersion slightly reduces the leading peak and trough. In the M_w9.0 MSZ megathrust event, the large rupture area generates longer tsunami waves, and the results given by the dispersive and non-dispersive models are almost identical.

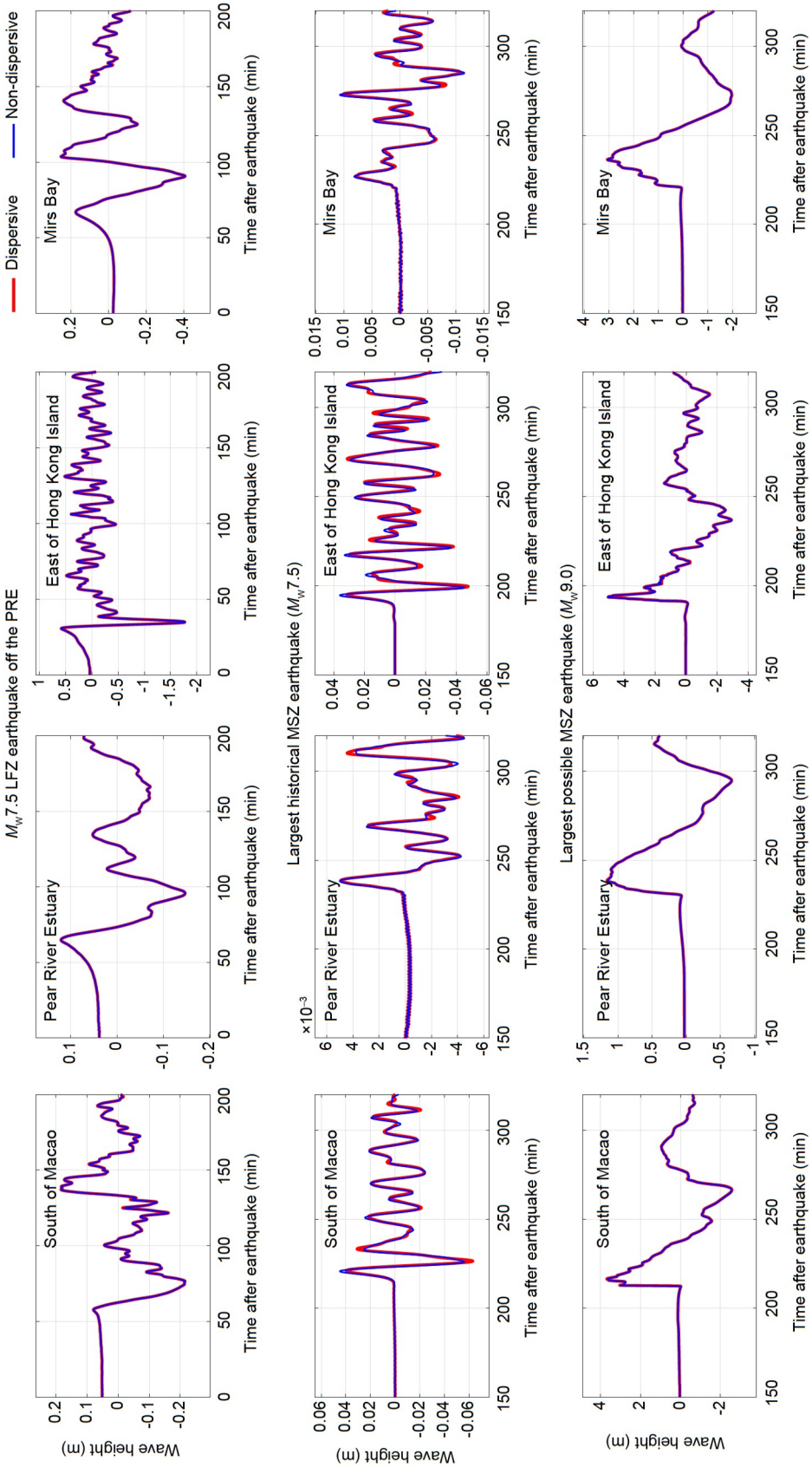

Figure 14 Comparison of tsunami waveforms calculated with dispersive and non-dispersive models.

5. Conclusions

In this study, we develop the parallel dispersive tsunami model PCOMCOT, which can efficiently simulate the entire life span of nonlinear, dispersive and breaking tsunami waves. This model is validated in a series of numerical tests, and shows satisfactory accuracy, stability and efficiency. For accurate modeling of tsunami hazards in the Greater Bay Area, we construct a high-resolution bathymetry dataset for the PRD, with special focus on Hong Kong and Macao. We then select two seismic zones—the LFZ and MSZ, as the potential tsunami source zones, and propose several presentative earthquake source models based on the results of dynamic rupture simulation, historical records and geodetic data. Subsequent tsunami propagation, transformation and run-up are accurately simulated, and the detailed characteristics of tsunami waves, currents and inundation in the GBA are analyzed. Our main conclusions about the potential tsunami hazards in the GBA are summarized as follows:

(1) Under control of the regional tectonic stress, the focal mechanisms of earthquakes in the PRE segment of LFZ may be right-lateral normal faulting. The tsunami generated by an M_w7.5 earthquake off the PRE would primarily impact the coast of Hong Kong, with maximum positive and negative waves of approximately 1 m and −2 m, respectively. Due to the complex effects of the Dangan Islands, the coastline and the continental slope on tsunami waves, there will be persistent sea surface oscillations of ~0.5 m around Hong Kong, while the area to the east and west will experience multiple long-period tsunami waves of less than 0.3 m. Besides, tsunami currents of >1.5 m/s, which are slightly destructive, will appear in several narrow waterways.

(2) The M_w9.0 MSZ megathrust event can generate tsunami waves of ~6 m in the PRE. The tsunami waves decay rapidly after entering the estuary, and inundation hazards mainly occur in Macao and Hong Kong on both sides of the PRE. The coastlines of Macao's outlying islands are flooded to a variable extent, with the inundation depth reaching up to 5 m at the southernmost tip of Coloane. In Hong Kong, the maximum inundation depth of ~6 m occurs in the Tai Long Wan. The dense urban areas around the Victoria Harbour are also significantly inundated, particularly at the Junk Bay and Chai Wan, where extensive inundation with depth of 1–2 m occurs.

(3) In addition to inundation hazards, MSZ megathrust earthquakes can induce catastrophic tsunami currents in the GBA. Extensive tsunami currents of >3 m/s will occur to the east of Macao's outlying islands. In the narrowest areas between Coloane and the Great Hengqin Island, as well as between the airport and Coloane, the localized currents are as fast as 6 m/s. In Hong Kong, strong currents of >2 m/s occur throughout the Victoria Harbour, with the local speed exceeding 5 m/s at the southeastern entrance. Moreover, a considerable discrepancy is observed between the spatial distributions of tsunami currents and inundated areas, suggesting the necessity to consider the risk of tsunami currents in tsunami hazard assessment.

Acknowledgements *This work was supported by the National Natural Science Foundation of China (Grant Nos. U1901602, T2122012) and the National Key R&D Program of China (Grant No. 2022YFC3003504).*

Conflict of interest The authors declare that they have no conflict of interest.

References

An C. 2021. Tsunamis and tsunami warning: Recent progress and future prospects. Sci China Earth Sci, 64: 191–204
An C, Sepúlveda I, Liu P L F. 2014. Tsunami source and its validation of the 2014 Iquique, Chile, earthquake. Geophys Res Lett, 41: 3988–3994
An C, Liu H, Ren Z, Yuan Y. 2018. Prediction of tsunami waves by uniform slip models. J Geophys Res-Oceans, 123: 8366–8382
Anderson E M. 1951. The Dynamics of Faulting and Dyke Formation with Applications to Britain. 2nd ed. Edinburgh: Oliver and Boyd
Aranguiz R, Catalán P A, Cecioni C, Bellotti G, Henriquez P, González J. 2019. Tsunami resonance and spatial pattern of natural oscillation modes with multiple resonators. J Geophys Res-Oceans, 124: 7797–7816
Baba T, Takahashi N, Kaneda Y, Ando K, Matsuoka D, Kato T. 2015. Parallel implementation of dispersive tsunami wave modeling with a nesting algorithm for the 2011 Tohoku tsunami. Pure Appl Geophys, 172: 3455–3472
Bai Y, Cheung K F, Yamazaki Y, Lay T, Ye L. 2014. Tsunami surges around the Hawaiian Islands from the 1 April 2014 North Chile M_w8.1 earthquake. Geophys Res Lett, 41: 8512–8521
Barrett R, Berry M, Chan T F, Demmel J, Donato J, Dongarra J, Eijkhout V, Pozo R, Romine C, Van der Vorst H. 1994. Templates for the Solution of Linear Systems: Building Blocks for Iterative Methods. 2nd ed. Philadelphia: Society for Industrial and Applied Mathematics
Bautista B C, Bautista M L P, Oike K, Wu F T, Punongbayan R S. 2001. A new insight on the geometry of subducting slabs in northern Luzon, Philippines. Tectonophysics, 339: 279–310
Borrero J C, Bell R, Csato C, DeLange W, Goring D, Dougal Greer S, Pickett V, Power W. 2013. Observations, effects and real time assessment of the March 11, 2011 Tohoku-oki tsunami in New Zealand. Pure Appl Geophys, 170: 1229–1248
Briggs M J, Synolakis C E, Harkins G S, Green D R. 1995. Laboratory experiments of tsunami runup on a circular island. Pure Appl Geophys, 144: 569–593
Cao J, Sun J, Xu H, Xia S. 2014. Seismological features of the littoral fault zone in the Pearl River Estuary (in Chinese with English abstract). Chin J Geophys, 57: 498–508
Cao J, Xia S, Sun J, Zhao F, Wan K, Xu H. 2018. Offshore fault geometrics in the Pearl River Estuary, Southeastern China: Evidence from seismic reflection data. J Ocean Univ China, 17: 799–810
Chen E, Huang Y. 1989. Characteristics of the seismic damage and analysis of the seismic structure of the 1605 great earthquake of Qiongzhou, Hainan island (in Chinese with English abstract). Acta Seismol Sin,11: 319–331
Chen H, He X, Yang H, Zhang J. 2021. Fault-plane determination of the 4 January 2020 offshore Pearl River Delta earthquake and its implication for seismic hazard assessment. Seismol Res Lett, 92: 1913–1925
Chen Q, Kirby J T, Dalrymple R A, Kennedy A B, Chawla A. 2000. Boussinesq modeling of wave transformation, breaking, and runup. II: 2D. J Waterway Port Coast Ocean Eng, 126: 48–56
De Almeida G A M, Bates P, Freer J E, Souvignet M. 2012. Improving the

stability of a simple formulation of the shallow water equations for 2-D flood modeling. Water Resour Res, 48: 2011WR011570
Fujii Y, Satake K. 2007. Tsunami source of the 2004 Sumatra–Andaman earthquake inferred from tide gauge and satellite data. Bull Seismol Soc Am, 97: S192–S207
Fujii Y, Satake K, Sakai S, Shinohara M, Kanazawa T. 2011. Tsunami source of the 2011 off the Pacific coast of Tohoku earthquake. Earth Planet Sp, 63: 815–820
Fujiwara T, Kodaira S, No T, Kaiho Y, Takahashi N, Kaneda Y. 2011. The 2011 Tohoku-oki earthquake: Displacement reaching the trench axis. Science, 334: 1240
Glimsdal S, Pedersen G K, Harbitz C B, Løvholt F. 2013. Dispersion of tsunamis: Does it really matter? Nat Hazards Earth Syst Sci, 13: 1507–1526
Gutenberg B, Richter C F. 1954. Seismicity of the Earth and Associated Phenomena. 2nd ed. Princeton: Princeton University Press
Harris R A, Barall M, Aagaard B, Ma S, Roten D, Olsen K, Duan B, Liu D, Luo B, Bai K, Ampuero J, Kaneko Y, Gabriel A, Duru K, Ulrich T, Wollherr S, Shi Z, Dunham E, Bydlon S, Zhang Z, Chen X, Somala S N, Pelties C, Tago J, Cruz-Atienza V M, Kozdon J, Daub E, Aslam K, Kase Y, Withers K, Dalguer L. 2018. A suite of exercises for verifying dynamic earthquake rupture codes. Seismol Res Lett, 89: 1146–1162
Hayes G P, Moore G L, Portner D E, Hearne M, Flamme H, Furtney M, Smoczyk G M. 2018. Slab2, a comprehensive subduction zone geometry model. Science, 362: 58–61
Heidarzadeh M, Gusman A R. 2021. Source modeling and spectral analysis of the Crete tsunami of 2nd May 2020 along the Hellenic subduction zone, offshore Greece. Earth Planets Space, 73: 74
Hsu Y J, Yu S B, Song T R A, Bacolcol T. 2012. Plate coupling along the Manila subduction zone between Taiwan and northern Luzon. J Asian Earth Sci, 51: 98–108
Hsu Y J, Yu S B, Loveless J P, Bacolcol T, Solidum R, Luis Jr A, Pelicano A, Woessner J. 2016. Interseismic deformation and moment deficit along the Manila subduction zone and the Philippine fault system. J Geophys Res-Solid Earth, 121: 7639–7665
Hu C, Wu Y, An C, Liu H. 2020. A numerical study of tsunami generation by horizontal displacement of sloping seafloor. J Earthquake Tsunami, 14: 2050018
Hu F, Zhang Z, Chen X. 2016. Investigation of earthquake jump distance for strike-slip step overs based on 3-D dynamic rupture simulations in an elastic half-space. J Geophys Res-Solid Earth, 121: 994–1006
Huang T, Zhang H, Shi Y. 2023. Numerical simulation of landslide-generated tsunamis in lakes: A case study of the Xiluodu Reservoir. Sci China Earth Sci, 66: 393–407
Ida Y. 1972. Cohesive force across the tip of a longitudinal-shear crack and Griffith's specific surface energy. J Geophys Res, 77: 3796–3805
Kajiura K. 1963. The leading wave of a tsunami. Bull Earthq Res Inst, Univ Tokyo, 41: 535–571
Kang Y, Yang X, Chen X, Chen G, Zheng S. 2008. Inversion of stress field in Guangdong and its adjacent area (in Chinese with English abstract). Acta Seismol Sin, 30: 59–66
Kao H, Huang G C, Liu C S. 2000. Transition from oblique subduction to collision in the northern Luzon arc-Taiwan region: Constraints from bathymetry and seismic observations. J Geophys Res, 105: 3059–3079
Lau A Y A, Switzer A D, Dominey-Howes D, Aitchison J C, Zong Y. 2010. Written records of historical tsunamis in the northeastern South China Sea-challenges associated with developing a new integrated database. Nat Hazards Earth Syst Sci, 10: 1793–1806
Lay T, Ammon C J, Kanamori H, Yamazaki Y, Cheung K F, Hutko A R. 2011. The 25 October 2010 Mentawai tsunami earthquake (M_w7.8) and the tsunami hazard presented by shallow megathrust ruptures. Geophys Res Lett, 38: L06302
Li L, Switzer A D, Chan C H, Wang Y, Weiss R, Qiu Q. 2016. How heterogeneous coseismic slip affects regional probabilistic tsunami hazard assessment: A case study in the South China Sea. J Geophys Res-Solid Earth, 121: 6250–6272
Li L, Switzer A D, Wang Y, Chan C H, Qiu Q, Weiss R. 2018. A modest 0.5-m rise in sea level will double the tsunami hazard in Macao. Sci Adv, 4: eaat1180
Li L, Qiu Q, Li Z, Zhang P. 2022a. Tsunami hazard assessment in the South China Sea: A review of recent progress and research gaps. Sci China Earth Sci, 65: 783–809
Li L, Li F, Qiu Q, Li Z, Hui G. 2022b. Tsunami simulation of the 1918 Nan'ao earthquake and its implication (in Chinese with English abstract). Acta Scient Natural Univ Sunyat, 61: 27–38
Liu H, Zhao X, Wang B, Ren Z. 2015. Numercial modeling of tsunami wave and tsunami warning approach in the South China Sea (in Chinese with English abstract). Chin Quart Mechan, 36: 351–369
Liu P L F, Cho Y S, Briggs M J, Kanoglu U, Synolakis C E. 1995. Runup of solitary waves on a circular Island. J Fluid Mech, 302: 259–285
Liu P L F, Woo S B, Cho Y S. 1998. Computer Programs for Tsunami Propagation and Inundation. Technical Report. Cornell University
Liu P L F, Wang X, Salisbury A J. 2009. Tsunami hazard and early warning system in South China Sea. J Asian Earth Sci, 36: 2–12
Liu Y. 1981. Fault Structure Analysis Along Southern Coast of China (in Chinese). Beijing: Seismological Press
Liu Y, Santos A, Wang S M, Shi Y, Liu H, Yuen D A. 2007. Tsunami hazards along Chinese coast from potential earthquakes in South China Sea. Phys Earth Planet Inter, 163: 233–244
Lynett P J, Borrero J, Son S, Wilson R, Miller K. 2014. Assessment of the tsunami-induced current hazard. Geophys Res Lett, 41: 2048–2055
Lynett P, Weiss R, Renteria W, De La Torre Morales G, Son S, Arcos M E M, MacInnes B T. 2013. Coastal impacts of the March 11th Tohoku, Japan tsunami in the Galapagos Islands. Pure Appl Geophys, 170: 1189–1206
Madsen P A, Sørensen O R, Schäffer H A. 1997. Surf zone dynamics simulated by a Boussinesq type model. Part I. Model description and cross-shore motion of regular waves. Coast Eng, 32: 255–287
Megawati K, Shaw F, Sieh K, Huang Z, Wu T R, Lin Y, Tan S K, Pan T C. 2009. Tsunami hazard from the subduction megathrust of the South China Sea: Part I. Source characterization and the resulting tsunami. J Asian Earth Sci, 36: 13–20
Mei C C. 1989. The Applied Dynamics of Ocean Surface Waves. Singapore: World Scientific
Nwogu O. 1993. Alternative form of Boussinesq equations for nearshore wave propagation. J Waterway Port Coast Ocean Eng, 119: 618–638
Okada Y. 1985. Surface deformation due to shear and tensile faults in a half-space. Bull Seismol Soc Am, 75: 1135–1154
Okal E A, Fritz H M, Raad P E, Synolakis C, Al-Shijbi Y, Al-Saifi M. 2006a. Oman field survey after the December 2004 Indian Ocean tsunami. Earthq Spectra, 22: 203–218
Okal E A, Fritz H M, Raveloson R, Joelson G, Pančošková P, Rambolamanana G. 2006b. Madagascar field survey after the December 2004 Indian Ocean tsunami. Earthq Spectra, 22: 263–283
Okal E A, Synolakis C E, Kalligeris N. 2011. Tsunami simulations for regional sources in the South China and adjoining seas. Pure Appl Geophys, 168: 1153–1173
Peng C, Li Y, Wu M. 2017. Analysis of seismogenic structure mechanism of the Nanao earthquake in 1918 (in Chinese with English abstract). South China J Seismol, 37: 1–14
Peregrine D H. 1967. Long waves on a beach. J Fluid Mech, 27: 815–827
Rangin C, Stephan J F, Blanchet R, Baladad D, Bouysee P, Min Pen C, Chotin P, Collot J Y, Daniel J, Drouhot J M, Marchadier Y, Marsset B, Pelletier B, Richard M A, Tardy M. 1988. Seabeam survey at the southern end of the Manila trench. Transition between subduction and collision processes, offshore Mindoro Island, Philippines. Tectonophysics, 146: 261–278
Ren Y, Wen R, Zhang P, Yang Z, Pan R, Li X. 2017. Implications of local sources to probabilistic tsunami hazard analysis in south Chinese coastal area. J Earthquake Tsunami, 11: 1740001
Ren Z, Gao Y, Ji X, Hou J. 2022. Deterministic tsunami hazard assessment and zoning approach using far-field and near-field sources: Study of Cixi County of Zhejiang Province, China. Ocean Eng, 247: 110487
Repetti W C. 1946. Catalogue of Philippine earthquakes, 1589-1899. Bull

Seismol Soc Am, 36: 133–322
Saito T, Ito Y, Inazu D, Hino R. 2011. Tsunami source of the 2011 Tohoku-oki earthquake, Japan: Inversion analysis based on dispersive tsunami simulations. Geophys Res Lett, 38: L00G19
Satake K, Fujii Y, Harada T, Namegaya Y. 2013. Time and space distribution of coseismic slip of the 2011 Tohoku earthquake as inferred from tsunami waveform data. Bull Seismol Soc Am, 103: 1473–1492
Sepúlveda I, Liu P L-F, Grigoriu M. 2019. Probabilistic tsunami hazard assessment in South China Sea with consideration of uncertain earthquake characteristics. J Geophys Res-Solid Earth, 124: 658–688
Sepúlveda I, Haase J S, Liu P L-F, Grigoriu M, Winckler P. 2021. Non-stationary probabilistic tsunami hazard assessments incorporating climate-change-driven sea level rise. Earths Future, 9: e2021EF002007
Shi F, Kirby J T, Harris J C, Geiman J D, Grilli S T. 2012. A high-order adaptive time-stepping TVD solver for Boussinesq modeling of breaking waves and coastal inundation. Ocean Model, 43-44: 36–51
Stelling G, Zijlema M. 2003. An accurate and efficient finite-difference algorithm for non-hydrostatic free-surface flow with application to wave propagation. Numer Methods Fluids, 43: 1–23
Sun J, Xu H, Zhan W, Cao J. 2012. Activity and triggering mechanism of seismic belt along the northern South China Sea continental margin (in Chinese with English abstract). J Trop Oceanogr, 3: 43–50
Tanioka Y, Satake K. 1996. Tsunami generation by horizontal displacement of ocean bottom. Geophys Res Lett, 23: 861–864
Van der Vorst H A. 1992. Bi-CGSTAB: A fast and smoothly converging variant of Bi-CG for the solution of nonsymmetric linear systems. SIAM J Sci Stat Comput, 13: 631–644
Wang L, Wang B, Ye X, Zhang Y, Wang X, Lu Z. 2021. An improved minimum 1-D V_P velocity model in the onshore-offshore area of the Pearl River estuary from 3-D active source seismic experiment (in Chinese with English abstract). Seismol Geol,43: 123–143
Wang P, Shan D, Wang G, Yu F, Hou J, Zhao L, Yuan Y, Fan T, Ren Z, Wang Z. 2016. Modelling and assessment of tsunami-induced vortex flows hazards from the 2011 M_w9.0 Tohoku-oki earthquake in harbors and adjacent area (in Chinese with English abstract). Chin J Geophys, 59: 4162–4177
Wang X. 2009. User Manual for COMCOT version 1.7 (FIRST DRAFT)
Wang X, Liu P L F. 2006. An analysis of 2004 Sumatra earthquake fault plane mechanisms and Indian Ocean tsunami. J Hydraulic Res, 44: 147–154
Wen R, Ren Y, Li X, Pan R. 2011. Probability analysis method of earthquake-induced tsunami risk in China (in Chinese with English abstract). South China J Seismol, 31: 1–13
Wesnousky S G. 2006. Predicting the endpoints of earthquake ruptures. Nature, 444: 358–360
Williamson A, Melgar D, Rim D. 2019. The effect of earthquake kinematics on tsunami propagation. J Geophys Res-Solid Earth, 124: 11639–11650
Wilson R I, Admire A R, Borrero J C, Dengler L A, Legg M R, Lynett P, McCrink T P, Miller K M, Ritchie A, Sterling K, Whitmore P M. 2013. Observations and impacts from the 2010 Chilean and 2011 Japanese tsunamis in California (USA). Pure Appl Geophys, 170: 1127–1147
Xu H, Qiu X, Zhao M, Sun J, Zhu J. 2006. The charateristics of crustal structure and seismogenic zone of the Nanao earthquake (M=7.5) in the northeastern South China Sea (in Chinese). Chin Sci Bull, 51: 83–91
Xu H, Ye C, Qiu X, Sun J, Xia S. 2010. Deep geophysical survery and investigation of the seismogenic structure of the littoral fault zone in the nothern South China Sea (in Chinese with English abstract). South China J Seismol, 30: 10–18
Xu Q. 2007. The land sank into the sea and possible tsunami by the great earthquake in Qiongzhou in China in 1605 (in Chinese). Acta Oceanol Sin, 29: 146–156
Yamazaki Y, Kowalik Z, Cheung K F. 2009. Depth-integrated, non-hydrostatic model for wave breaking and run-up. Numer Methods Fluids, 61: 473–497
Yang T F, Lee T, Chen C H, Cheng S N, Knittel U, Punongbayan R S, Rasdas A R. 1996. A double island arc between Taiwan and Luzon: Consequence of ridge subduction. Tectonophysics, 258: 85–101
Yuan Y, Li H, Wei Y, Shi F, Wang Z, Hou J, Wang P, Xu Z. 2021. Probabilistic tsunami hazard assessment (PTHA) for southeast coast of Chinese mainland and Taiwan island. J Geophys Res-Solid Earth, 126: e2020JB020344
Zhang W, Chen X. 2006. Traction image method for irregular free surface boundaries in finite difference seismic wave simulation. Geophys J Int, 167: 337–353
Zhang W, Shen Y, Chen X F. 2008. Numerical simulation of strong ground motion for the M_s8.0 Wenchuan earthquake of 12 May 2008. Sci China Ser D-Earth Sci, 51: 1673–1682
Zhang Z, Zhang W, Chen X. 2014. Three-dimensional curved grid finite-difference modelling for non-planar rupture dynamics. Geophys J Int, 199: 860–879
Zhang Z, Zhang W, Chen X, Li P ', Fu C. 2017. Rupture dynamics and ground motion from potential earthquakes around Taiyuan, China. Bull Seismol Soc Am, 107: 1201–1212
Zhang Z, Zhang W, Chen X. 2019. Dynamic rupture simulations of the 2008 M_w7.9 Wenchuan earthquake by the curved grid finite-difference method. J Geophys Res-Solid Earth, 124: 10565–10582
Zhu Y, An C, Wang T, Liu H. 2021. Time-dependent tsunami source following the 2018 Anak Krakatau volcano eruption inferred from nearby tsunami recordings. China Ocean Eng, 35: 145–152

(Editorial handling: Yong ZHENG)